Numerical model of the behavior of chlorinated ethenes in a fractured, karstic limestone aquifer

Nicola Pastore [1] · Claudia Cherubini [2] · Concetta I. Giasi [1] · Dimitra Rapti [2]

Abstract

Characterizing the transport and degradation of chlorinated ethenes in fractured aquifers, as well as the assessment of cleanup times, poses an extreme technical challenge. In the presented study, a method to analyze reactive transport and reductive dechlorination of chlorinated solvents in fractured aquifers is developed. A rough-walled parallel-plate model of nonlinear flow behavior is coupled with random-walk particle tracking, incorporating particle exchange between the mobile and stagnant zones, adsorption processes, and reductive dechlorination reaction pathways. The developed methodology, considering reductive dechlorination processes in a Lagrangian framework, is able to simulate the motion of particles affected by first-order network reactions, so that particles move according to their chemical state, affecting physical transport processes (advection, dispersion, mass-transfer exchange between mobile and stagnant zones). The developed model is applied to a case study of groundwater contamination in the industrial area of Bari and Modugno (Italy), where the limestone aquifer has a fractured, karstic nature. The steady-state distribution of the contamination by chlorinated ethenes from a source at a hot spot is obtained and compared with the observed scenario of contamination, in order to estimate the plausible transport and degradation processes and the mass loading at source. The study represents a valuable tool in deciding the role of natural attenuation as a treatment option, where the natural attenuation capacity of groundwater can be integrated with engineering methods in order to obtain site remediation.

Keywords Chlorinated ethenes · Fractured rocks · Random particle tracking

Introduction

Chlorinated ethenes (CEs) have been widely used as solvents in manufacturing operations and they represent the most frequently detected contaminants in groundwater. Their behavior and bioremediation in unconsolidated aquifers composed of granular materials (e.g., sand, silt and gravel) have been extensively assessed for several decades (Yu 2017). As most bioremediation studies have taken place in granular porous media, there is scarce information on the use of bioremediation for in situ treatment of CEs in fractured bedrock (Pérez-de-Mora et al. 2014).

Fractured bedrock presents a significant remediation challenge. Matrix diffusion and dead-end fractures could act as the primary storage place for contaminants. The diffusion of contaminants from the mobile water in the fractures to the virtually stagnant water within the rock matrix can make aquifer restoration frustratingly slow at best, and at worst, an exercise in futility (Mutch et al. 1993). Furthermore, matrix diffusion and stagnant zones play an important role on the CEs' persistence after bioremediation activity (Verce et al. 2015). On the other hand, dechlorinated microorganisms have been detected in the rock matrices away from fracture surfaces, indicating that biodegradation within the rock matrix blocks should be considered as an important component for the evaluation of the natural attenuation potential or remediation (Lima et al. 2012). Groundwater flow-path characterization is essential in order to assess the variability of natural attenuation processes

✉ Nicola Pastore
nicola.pastore@poliba.it

✉ Claudia Cherubini
claudia.cherubini@unife.it

[1] Polytechnic of Bari, Department of Civil, Environmental and Structural Engineering and Chemistry (DICATECh), via E. Orabona 4, 70125 Bari, Italy

[2] Department of Physics and Earth Sciences, University of Ferrara, via Saragat 1, 44122 Ferrara, Italy

of CEs in fractured rock systems (Bradley et al. 2009). In fractured rock aquifers, groundwater flow pathways also govern the hydraulic connectivity and travel time between wells for recirculation of remediation fluids in an enhanced natural attenuation (ENA) cleanup strategy (Verce et al. 2015). In fracture-dominated flow regimes, the extent of injection and distribution of remediation countermeasures could not be conceptualized using simple homogeneous models of groundwater flow commonly adopted to design injections in less heterogeneous unconsolidated geologic materials (Tiedeman et al. 2018).

Generally, natural attenuation of CEs is favored under anaerobic conditions in the presence of iron-reduction, sulfate-reduction and methanogenesis redox conditions (Lenczewski et al. 2003). Chemical reactions that involve CEs, electron acceptor and donor organic matter, and microorganisms can be complex but predictable. Many researchers faced the challenging issue of studying dechlorination of CEs in fractured aquifers when carrying out field investigations, laboratory tests and numerical simulations (Yager 2002, Manoli et al. 2012; Pérez-de-Mora et al. 2014; Şimşir et al. 2017). When contaminant concentrations are small (i.e. less than the half-saturation constant in the Monod model) transformation rates of CEs can be described by pseudo first–order reaction rates (Yager 2002; Burnell et al. 2014).

The interactions between the heterogeneity and anisotropy of aquifer properties, diffusion in stagnant zones and chemical reactions often complicate reactive transport simulations (Henri and Fernàndez-Garcia 2015). In this situation, site-specific transport models—incorporating nonlinear flow, mass transfer between mobile and stagnant zones, sorption processes and reductive dechlorination pathways—are needed in order to evaluate natural attenuation potentials and/or clean up strategies.

In a general way, fractured and karst aquifers can be conceptualised as multiple-porosity media with a strong variation of the hydraulic properties, including media such as matrix pores, fractures and conduits, in which nonlinear flow can occur (Cheng and Chen 2005). Flow through fractures and/or conduits is often non-Darcian, which influences the flow dynamics and contaminant transport. Several researchers have investigated deviation of the cubic law of flow from observed flow behaviour, proposing correction factors and/or velocity dependent functions to take into account roughness of fracture walls and tortuosity (Zimmerman and Bodvarsson 1996; Waite et al. 1998; Cherubini et al. 2012; Cherubini et al. 2013a).

Connected fractures act as conduits for groundwater, whereas matrix diffusion and stagnant zones, due to the presence of dead-end channels and irregularities of fracture walls, trap the contaminated mass. This is later released with the result of anomalous discharge behavior characterized by an early arrival and long tailing (Lee et al. 2017; Dou et al. 2018). Non-Fickian behaviour has been associated with mass diffusion between the fracture and matrix (Zhou et al. 2006), the channeling effect due to variable apertures (Tsang and Tsang 1987), and stagnation zones near fracture walls (Cardenas et al. 2007).

Where the matrix porosity is low, the presence of recirculation zones may represent the main cause of non-Fickian transport, especially when nonlinear flow occurs influencing both (1) the advection that causes a delay in solute transport with respect to the linear flow assumption and (2) the stagnant zones that enhance the presence of eddies within the fractures, with a result of a persistence of the contaminant plume (Qian et al. 2011; Cherubini et al. 2013b, Cherubini et al. 2014; Lee et al. 2015).

In addition, the evolution of CEs in the groundwater environment involves reaction pathways, resulting commonly from biotic and/or abiotic anaerobic reductive dechlorination. In general, reaction pathways involved in the degradation of CEs do not follow the sequential reaction chain. First, the reductive dechlorination processes produce chloride. The complete dechlorination of 1 mol of tetrachloroethylene (PCE) corresponds to 4 mol of chloride (Semprini et al. 1990). Second, degradation of trichloroethylene (TCE) produces three daughter species: cis-1,2-dichloroethylene (cis-1,2-DCE), trans-1,2-dichloroethylene (trans-1,2-DCE) and 1,1-dichloroethylene (1,1-DCE) simultaneously (Wiedemeier et al. 1996). The reaction rates of DCEs are different, as well as their toxicity. Third, abiotic degradation favors reductive ß-elimination, α-elimination and hydrogenation pathways (He et al. 2015); furthermore, the reaction rates in the mobile and stagnant zone can be substantially different (Cunningham and Mendoza-Sanchez 2006).

The sorption processes of chlorinated solvents and their degradation products are different. Highly CEs (PCE and DCE) present a stronger sorption behaviour then lower CEs such as DCEs and vinyl chloride (VC). Assuming a linear isotherm is valid, the retardation factors of each CEs and their degradation products such as ethylene (ETH) can be different, affecting transport mechanisms such as advection and the interaction between the mobile and stagnant zones (Lu et al. 2011). As a consequence, the fate and transport processes of CEs in fractured media could become complicated.

Particle-based methods represent an efficient numerical approach to simulating reactive transport (Kitanidis 1994; Salamon et al. 2006; Henri and Fernàndez-Garcia 2014). Several particle-based methods exist to simulate multispecies contaminant plumes affected by reaction networks limited to first-order kinetics (Burnell et al. 2014; Henri and Fernàndez-Garcia 2015) or with more complex kinetics (Benson and Bolster 2016; Engdahl et al. 2017; Sole-Mari et al. 2017).

The base concept of almost all of these approaches is that the single particle is viewed as an infinitely small plume (Kitanidis 1994) associated with a mobile bin containing the mass of each species associated with the single particle. Then

the single particle evolves from species i to species j according to a transition probability matrix. The particle moves according to an effective retardation factor, calculated as the harmonic mean between the species i and j involved in the chemical reaction. Some limitations attributed to these kinds of methods concern the use of very small times steps to represent linear sorption and the fact that chemical reactions must follow a sequential reaction pathway. The reaction network of CEs and their degradation products is simplified as a sequential reaction chain. The main disadvantage is linked to the fact that all DCEs are lumped together as single species and the evolution of their daughter species is not properly predicted.

In this paper, an efficient particle-based method to simulate transport and reductive dechlorination processes, including complete reaction pathways, is developed. The approach approximates reductive dechlorination processes as first-order-kinetics reaction pathways in combination with a nonlinear flow model, dependent on velocity-field mass-transfer processes between mobile and stagnant zones and linear sorption. The developed method takes the spatial heterogeneity of aquifer characteristics into account in terms of advection, dispersion, linear sorption and mass transfer processes, as well as the degradation efficiency of the CEs by means of the definition of the redox zones. The developed method associates with the particles, which enter into a generic redox zone at a specific time, and a mass distribution vector containing the total mass associated with each species. The mass distribution vector evolves in time according to the imposed reaction pathways, which do not necessarily follow a sequential reaction chain (generic species i can evolve into one or more species). Particle-transition probabilities are determined according to the mass consumed in the time interval. Finally, the particle species change according to the transition probabilities using a Markov chain model. In this way, to each particle is associated a single species that does not necessarily change according to a sequential chain. The retardation factor associated with each particle depends on the sorption characteristics of the single species associated with it (distribution coefficient) as well as its position in the space domain, which determines the aquifer characteristics.

The developed method is applied to the case study of the fractured, karst limestone aquifer of the industrial area of Bari (Italy). Previous studies carried out on the same aquifer have applied different conceptual, mathematical and numerical models to model the fluid flow (Cherubini et al. 2013a; Cherubini et al. 2018), conservative transport (Masciopinto and Palmiotta 2013), reactive transport (Masciopinto et al. 2010) and variable density flow (Masciopinto and Palmiotta 2016; Masciopinto et al. 2017). Some of them are used to set up the flow model that determines the flow field. This work was developed from the two-dimensional (2D) flow model presented by Cherubini et al. (2018), who coupled a rough-walled

parallel-plate model for flow simulation with inverse modeling and geostatistical analysis, to infer the value of the equivalent transmissivity distribution. In the present work, the flow model has been calibrated on the basis of the point dilution tests presented in Masciopinto and Palmiotta (2016). Furthermore, the experimental breakthrough curve (BTC) obtained from the forced-gradient test presented in Masciopinto and Palmiotta 2013 has been used to analyse the mass exchange behaviour between the mobile and stagnant zone, as well as to estimate the mass exchange parameters comparing the observed data with simulated data.

The specific goals of this paper are to:

1. Test if the developed particle-based approach can adequately represent the scenario of contamination in the study area.
2. Analyze if the natural attenuation strategies represent a valid alternative for aquifer remediation.
3. Enrich understanding of the hydrogeological behavior of the aquifer, highlighting how the heterogeneity, anisotropy, nonlinear flow and mass transfer processes affect the scenario of contamination and the remediation strategy.

Materials

Field site

The industrial site of Bari is a flat area with the highest elevation of 30 m above sea level (asl), facing the Adriatic Sea in southeastern Italy, with an areal extent of 1,509 ha. More than 800 industries are present, among which 20 are multinational companies. The industrial activities involve several sectors: food, chemicals, petrochemicals, textiles, wood, mechanics, mechatronics, information and communication technology (ICT), lamp production and building.

The observed annual mean temperature is between 14.4 and 20.4 °C. The area has a semiarid climate with annual average rainfall and potential evapotranspiration of 540 and 1,063 mm respectively.

From the morphological point of view, the study area is a typical coastal Murgian belt characterized by the presence of wide elongated terraces parallel to the coast and gentle slopes to the sea, ending on the waterside with marine terraces bordered by low escarpments. Three-tiered terraces are detectable sloping down to the sea with elevations between 40 and 10 m asl, characterized by paleostream channels or small erosive furrows (called in the Apulian region "lame") perpendicular to the terraces (Fig. 1).
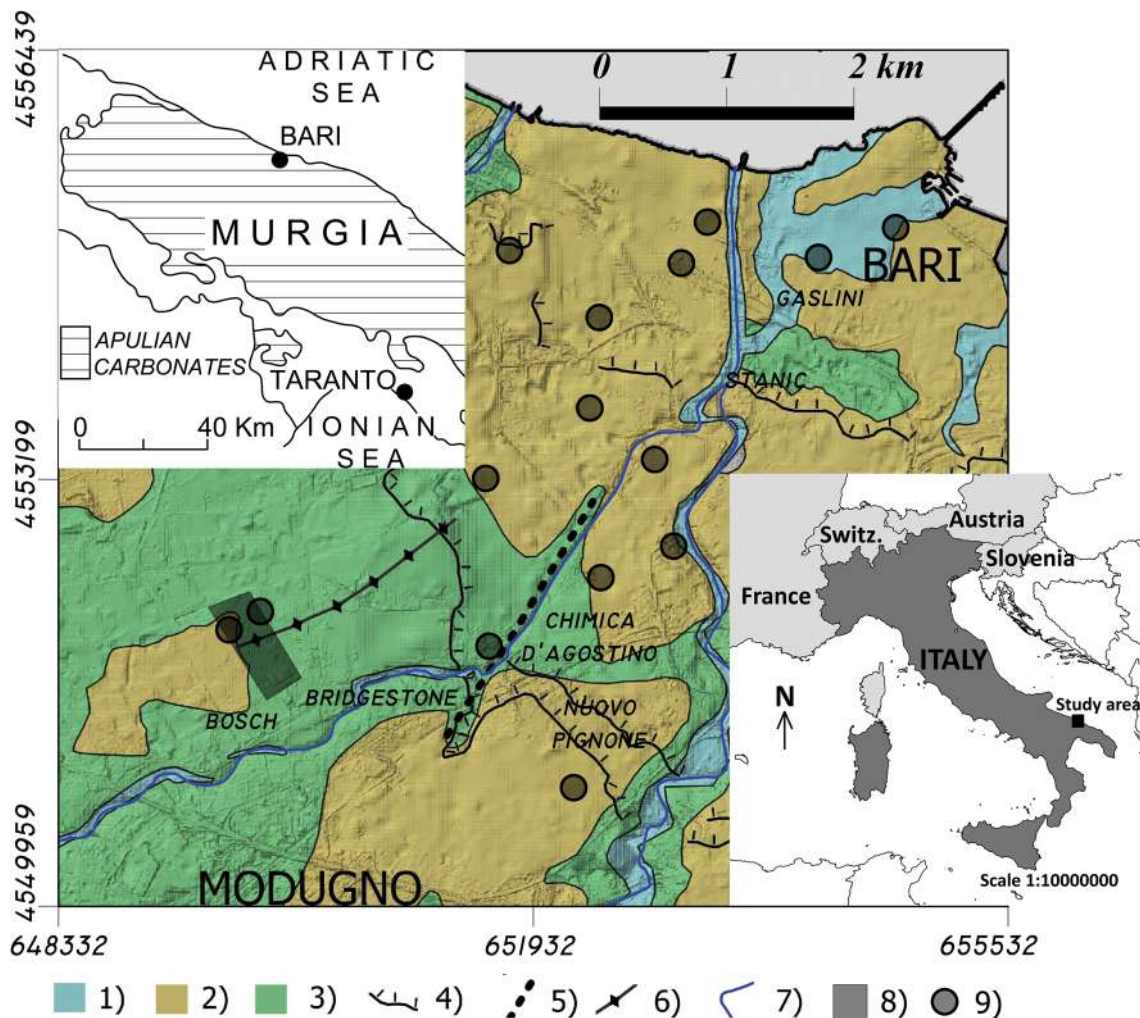
Fig. 1 Geological map of the industrial area of Bari, southeastern Italy. Legend: 1 alluvial and marshy deposits (Holocene); 2 Calacareniti di Gravina Formation (lower Pleistocene); 3 Calcare di Bari formation (Cretaceous); 4 escarpments; 5 fault (uncertain); 6 anticlinal axis; 7 hydrographic network; 8 potential source area of contamination; 9 location of the monitoring wells

Evidence of dechlorination processes

In the study area, a diffusive contamination by chlorinated aliphatic hydrocarbons—PCE, TCE, 1,1-DCE, cis & trans 1,2-DCE and VC—has been detected, which is being transported downgradient from the potential source area of contamination toward the coastal area in the SW–NE direction.

Tetrachloroethylene represents about 80% of the total CEs at the hot-spot area, whereas TCE has been detected at lower concentrations than PCE in all locations. The amount of 1,2-DCE is greater than 80% of the total DCE, representing an indicator of the presence of dechlorination processes.

The greatest biodegradation efficiency of the highest-chlorinated CEs is found under methanogenic/sulfidogenic groundwater conditions. The detected redox potential value is consistent with the presence of iron-reducing conditions where the fracture coating, composed by red soil, represents

a source of ferric iron (Fe^{3+}) in the redox reaction. However, this scenario is not consistent with the detected concentration of ferrous iron (Fe^{2+}), below 20 $\mu g\,L^{-1}$, and the high concentration of nitrate (above 1 mg L^{-1}), but represents the highest electron acceptor (EC) after the dissolved oxygen. More details on CEs and EAs characterization are reported in the electronic supplementary material (ESM).

Geological and hydrogeological setting

From the geological viewpoint (below the top soil), the study area is characterized by the presence of alluvial and marshy deposits (Holocene) at the bottom of the lame and some depressions in the dune deposits, and by the presence of Calcareniti di Gravina formation (lower Pleistocene) with a variable thickness from few meters to 20 m. It is a calcarenitic complex, transgressive on the underlying formation, sometimes in angular discordance, constituted by dune bioclastic,

detritic and sand-bar deposits constituted by calcarenites with marine fossils, volcanic sands and sandstones, and discontinuous layers of gravel and conglomerates. Below the calcarenitic strata lies the Calcare di Bari formation, represented by a Cretaciceous calcareous dolomitic succession extending in depth for hundreds of meters. The succession consists of biopeloidal and peloidal wackestones/packstones alternating with stromatolithic bindstones with frequent intercalations of dolomitic limestones and grey dolostones. This succession appears stratified and fissured and, where it is not intersected by tectonic discontinuities, it shows a subhorizontal or slightly inclined attitude (Maggiore 1993).

From the hydrogeological point of view, the study area belongs to the karstic Murgia aquifer, characterised by calcareous lithotypes and having a secondary fissure-type permeability of tectonic origin. The prolonged karstic dissolution action of water on carbonate rocks has enlarged and interconnected the already existing discontinuities, creating a deep network of subterranean passages.

Inside the cavities of variable dimensions created by the complex and relevant karstic phenomena, conspicuous accumulations of red soil "terra rossa" can be detected. The origins of this residual material are not always attributable to its survey site. Dell'anna et al. (1985) and Vingiani et al. (2018) investigated the geochemical composition of terra rossa in the study area and detected silica and calcite (35–45%) kaolinite and illite (25–30%) and iron (10–15%) (hematite, magnetite and goethite) with small quantities of calcium oxides, potassium, titanium, magnesium, sodium, manganese and phosphorus.

Because of karstic phenomena, all the Murgian territory is characterized by scarce surface-water flow, even in the presence of an extensively developed hydrographic network. The local hydrographic network typical of the Apulian countryside is in fact constituted by the lame which act as ephemeral water courses. The high permeability of carbonatic rocks facilitates the infiltration of rainwater into the subsoil so that surface flow occurs only after very intense rain events. This implies the presence of a conspicuous and extended groundwater circulation in the subsoil, floating on underlying seawater of continental invasion.

One of the peculiar hydrogeological characteristics of the Murgia aquifer is the pronounced anisotropy linked to the different degree of fracturing and karst phenomenon of the carbonatic rocks that determines a high variability in the vertical and especially horizontal hydraulic conductivity, with values oscillating between 0.2 and 612 m day^{-1}, whereas rock porosity has values between 1.24 and 5.14% (Borgia et al. 2002).

The degree of fracturing affecting the Calcare di Bari formation is quite variable and mainly depends on the geological and structural (faults, anticline axis, etc.) evolution of the area, including faulting and folding. Borehole and in situ surveys carried out by private companies evidence the presence of two intervals: an upper level constituted by a carbonate rock sequence intensely fractured and karstified and 26 m thick, and a lower level represented by a dolomitic sequence >20 m thick which is less fractured and karstified.

In the study area, groundwater flows in the limestone Cretaceous formation within fractures and karst channels at variable depths from 40 m below the ground level in the most inland zone of the industrial area, up to about 12–13 m depth at its north-eastern border, with hydraulic head values of about 1–2 m above sea level. Groundwater flows in phreatic or semiconfined conditions mainly in the SW–NE direction perpendicular to the coastline, with hydraulic gradients of 0.1–0.5% (Grassi et al. 1986).

Methods

Conceptual model

Calcare di Bari formation is characterized by a succession of carbonate beds separated by marked subhorizontal mechanical discontinuities and affected by subvertical fractures with parted beds and unparted beds (Billi 2005) (Fig. 2a, b). Groundwater flows along the preferential channels due to the connectivity of the fractures, and the flow is influenced by the fracture aperture distribution and roughness. The presence of these preferential pathways favors both the transport of contaminants in groundwater along them and contaminant diffusion into stagnant zones represented by dead-end channels and/or eddies. Furthermore, at smaller scale, stagnant zones are also present in interaggregate pores and or biofilms attached to fracture surfaces. Dechlorination processes occur along the preferential flow pathways and stagnant zones in which substrate availability and nutrient supply are largest, enhancing microbial and geochemical processes.

A simple way to represent horizontal flow through a fractured aquifer is the well-known parallel-plate model (Huitt 1956; Snow 1965; Sarkar et al. 2004; Masciopinto et al. 2010). The fractured medium is conceptualised as a specific number n_f [−] of equivalent horizontal rough-walled parallel plates having the same mean aperture distribution, which varies along x and y directions $\overline{b}(x, y)$ (Fig. 2c).

The equivalent transmissivity of the fractured aquifer is also variable in space along the x and y directions, i.e. $T_{eq}(x, y)$; (Fig. 2d), and it can be linked to the parallel plates:

$$T_{eq}(x, y) = n_f \overline{T}_f(x, y) \tag{1}$$

where $\overline{T}_f(x, y)$ is the equivalent transmissivity distribution of each parallel plate.
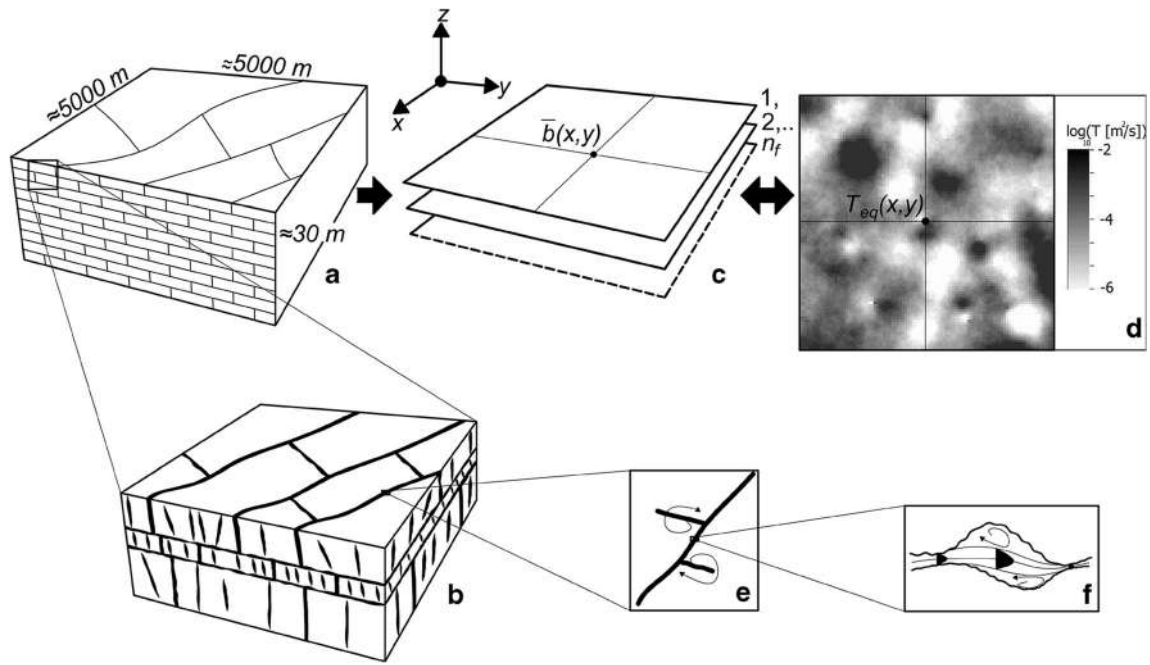
Fig. 2 **a** and **b** Sketch of the fracture network of the Calcare di Bari formation, **c** set of equivalent horizontal rough-walled parallel plates with the same mean aperture variable in space along the x and y direction, d hydraulic transmissivity map $[\log_{10} T\,(\mathrm{m\,s^{-1}})]$ linked to the parallel plates, **e** recirculation zones due to dead-end channels, **f** recirculation zones due to eddies

Parallel plates are characterised by the presence of a mobile zone (preferential pathways) and stagnant zones (Fig. 2e,f). The solute transport processes in saturated fractured limestone are modelled under dual-porosity model assumptions where a first-order mass exchange exists between the mobile zone and stagnant zones (Guan et al. 2008).

Flow model

Under the linear flow assumption, $\overline{T}_f(x,y)$ is proportional to the cubic power of the mean aperture distribution by means of the cubic law:

$$\overline{T}_f(x,y) = \frac{\rho g}{\mu}\frac{\overline{b}(x,y)}{12} \tag{2}$$

When the nonlinear flow condition occurs, $\overline{T}_f(x,y)$ is well represented by the Darcy–Weisbach equation:

$$\overline{T}_f(x,y) = \overline{b}(x,y)\sqrt{\frac{4\overline{b}(x,y)}{f(x,y)}g}\left(\sqrt{|\nabla h(x,y)|}\right)^{-1} \tag{3}$$

where g (L T^{-2}) is the gravity acceleration, h (L) is the hydraulic head and $f(-)$ is the friction factor. The latter is strongly dependent on the flow regime and, according to Nazridoust et al. (2006), assumes the following expression:

$$f(x,y) = \frac{123}{\mathrm{Re}(x,y)}\left[1 + 0.12\mathrm{Re}(x,y)^{0.687}\right] \tag{4}$$

where $\mathrm{Re}(x,y)$ is the Reynolds number distribution along the single parallel plate described as:

$$\mathrm{Re}(x,y) = \frac{\rho|\mathbf{v}(x,y)|2\overline{b}(x,y)}{\mu} \tag{5}$$

where ρ (ML^{-3}) is the density, μ (ML^{-1} T^{-1}) is the viscosity and $|\mathbf{v}(x,y)|$ is the module of the velocity vector distribution. The Darcy–Weisbach equation is close to the cubic law under linear flow conditions (Re < 1), with the friction factor distribution equal to $f(x,y) = 96/\mathrm{Re}(x,y)$.

The relationship between $\overline{T}_f(x,y)$, n_f and $\overline{b}(x,y)$ is not unique. Different combinations of n_f and $\overline{b}(x,y)$ could lead to similar values of $\overline{T}_f(x,y)$ with different velocity distributions. Furthermore, the presence of a nonlinear flow regime complicates even more the determination of the flow model parameters because transmissivity is dependent on the flow field.

Here a method to determine the flow velocity field is proposed. First, the equivalent transmissivity $T_{eq}(x,y)$ and the hydraulic head $h(x,y)$distribution under steady-state conditions must be determined by means of groundwater flow investigations, analysis and 2D flow modeling. Second, given a number of parallel plates, their respective mean aperture distribution $\overline{b}(x,y)$ and the velocity field $\mathbf{v}(x,y)$ in each single parallel plate are determined according to the following recursive equations:

$$\mathrm{Re}^k(x,y) = \frac{\rho\left|\mathbf{v}^k(x,y)\right|2\overline{b}^k(x,y)}{\mu}$$

$$f^{k+1}(x,y) = \frac{123}{\mathrm{Re}^k(x,y)}\left[1 + 0.12\,\mathrm{Re}^k(x,y)^{0.687}\right] \tag{6}$$

$$\overline{b}^{k+1}(x,y)\sqrt[3]{\frac{T_{\mathrm{eq}}}{n_{\mathrm{f}}^2}\frac{f^{k+1}(x,y)}{4g}}|\nabla h| \tag{7}$$

$$\mathbf{v}^{k+1}(x,y) = -n_{\mathrm{f}}\overline{b}(x,y)^{k+1}\frac{\sqrt{\dfrac{4\overline{b}^{k+1}(x,y)}{f^{k+1}(x,y)}g}}{\sqrt{|\nabla h(x,y)|}}\nabla h(x,y) \tag{8}$$

The recursive equations are initialised by determining the mean aperture distribution and the velocity field $\mathbf{v}(x,y)$ according to the cubic law:

$$\overline{b}(x,y) = \sqrt[3]{12\frac{T_{\mathrm{eq}}(x,y)}{n_{\mathrm{f}}}\frac{\mu}{\rho g}} \tag{9}$$

$$\mathbf{v}(x,y) = \frac{\rho g}{\mu}\frac{\overline{b}(x,y)}{12}\nabla h(x,y) \tag{10}$$

Finally, n_{f} is estimated according to the field flow-velocity observations. Point dilution tests have been used to estimate, at a specific location, the specific discharge $\mathbf{q}$ ($L^2\,T^{-1}$) which is defined, according to the conceptual model, as the product between the flow velocity $\mathbf{v}$ and the void area available for the flow equal to the product $n_{\mathrm{f}} \times \overline{b}$. Having estimated $\mathbf{q}$, given a value of n_{f}, the void area available for the flow must be equal to the ratio between the observed specific discharge and the velocity $\mathbf{v}$ determined at the location where the point dilution test has been conducted. The effective porosity or mobile porosity of the aquifer θ_{m} (−) is derived by the ratio between n_{f} $\times\overline{b}$ and the average aquifer thickness B (L). In this way a relationship between n_{f} and θ_{m} is obtained. Then the plausible value of n_{f} is obtained comparing the n_{f}–θ_{m} relationship and the value of the effective porosity observed in the field.

Solute transport and reductive dechlorination model

Assuming that changes in porosity are negligible in space and time and contaminant concentrations are small, such that pseudo-first-order reaction rates adequately represent the dechlorination processes, the groundwater transport of CEs and their degradation products in fractured rock (incorporating dual porosity effects, absorption and dechlorination processes) can be described by the following system of partial differential equations:

$$\frac{\partial c_{\mathrm{m}}^i}{\partial t} = \frac{1}{R_{\mathrm{m}}^i}\left[\nabla\cdot\left(\mathbf{v}c_{\mathrm{m}}^i - \mathbf{D}\nabla c_{\mathrm{m}}^i\right) + \alpha\left(c_{\mathrm{im}}^i - c_{\mathrm{m}}^i\right)\right] + \Lambda_{i,j=1,\ldots,n}\mathbf{c}_{\mathrm{m}}^T \quad i = 1,\ldots,n$$

$$\beta_i\frac{\partial c_{\mathrm{im}}^i}{\partial t} = -\frac{\alpha_i}{R_{\mathrm{m}}^i}(c_{\mathrm{im}}^i - c_{\mathrm{m}}^i) + \beta_i\left(\Lambda'_{i,j=1,\ldots,n}\mathbf{c}_{\mathrm{im}}^T\right) \tag{11}$$

where c_{m}^i and c_{im}^i [M L^{-3}] are the solute concentration for the i-th species in the mobile and stagnant (immobile) zones, $\mathbf{v}$ [L T^{-1}] is the velocity vector, $\mathbf{D}$ [L T^{-2}] is the symmetric dispersion tensor, R_{m}^i and R_{im}^i [−] are the retardation factor for the i-th species in the mobile and stagnant zones, α_i [T^{-1}] is the mass transfer coefficient between mobile and stagnant zones for the i-th species, β_i [−] is the capacity ratio for i-th species, and Λ (T^{-1}) and Λ' (T^{-1}) are the reaction network matrix for the mobile and stagnant zone respectively.

The symmetric dispersion tensor has the following components:

$$\begin{aligned} D_{xx} &= \left(\alpha_{\mathrm{L}}v_x^2 + \alpha_{\mathrm{T}}v_y^2\right)/|\mathbf{v}|,\\ D_{yy} &= \left(\alpha_{\mathrm{T}}v_x^2 + \alpha_{\mathrm{L}}v_y^2\right)/|\mathbf{v}|,\\ D_{xy} &= (\alpha_{\mathrm{L}}-\alpha_{\mathrm{T}})v_xv_y/|\mathbf{v}| \end{aligned} \tag{12}$$

where α_{L} and α_{T} are the longitudinal and transverse dispersivities, respectively.

Sorption processes of organic compounds occur at the fracture walls due to the presence of iron oxides in red soil. The retardation factor accounting for the sorption of the solute onto the fracture walls, both for mobile and stagnant zones, are respectively defined as:

$$R_{\mathrm{m}}^i(x,y) = 1 + fK_{\mathrm{a}}^i a(x,y) \qquad R_{\mathrm{im}}^i = 1 + (1-f)K_{\mathrm{a}}^i a(x,y) \tag{13}$$

K_{a}^i [L] is the surface distribution coefficient of the i-th species which indicates the extent of sorption relative to the surface area of the fracture walls available for sorption, f is the mass fraction of sorbed phase in the sorption equilibrium within the mobile zone, $a(x, y)$ [L^{-1}] is the surface-area to volume ratio of the fracture system which is variable in space along x and y directions. For the parallel plate model, $a(x, y)$ is equal to $2/\overline{b}(x,y)$. The surface distribution coefficient can be derived by the ratio between the partition coefficient K_{d} ($L^3\,M^{-1}$) associated with the i-th species and the internal specific surface area of the rock γ ($L^2\,M^{-1}$) defined by Novakowski (1999) as:

$$\gamma = \frac{2\theta}{\delta\rho_{\mathrm{b}}} \tag{14}$$

where θ is the rock porosity, ρ_{b} (M L^{-3}) is the bulk density of the reactive material (red soil) and δ is the geometric factor representing the arrangement of the pore space (Freeze and Cherry 1979).

K_d (L^3 M^{-1}) of each i-th species is equal to the product of the fraction of organic carbon present in the reactive soil and the K_{oc}.

The capacity ratio associated with each species is given by:

$$\beta_i(x,y) = \frac{\theta_{im}R_{im}^i(x,y)}{\theta_m R_m^i(x,y)} \tag{15}$$

where θ_{im} represents the porosity of stagnant zones.

Experimental evidence shows that the mass transfer coefficient depends on the velocity field (Cherubini et al. 2013b). The increase of Re lead to eddies growth increasing the recirculation zones. Therefore, the mass transfer coefficient is variable in space along the x and y directions on the basis of the experimental potential law derived by Cherubini et al. (2013b) between α and Re:

$$\alpha(x,y) = 2\cdot10^{-3} + 1.1\cdot10^{-5}Re^2(x,y) \tag{16}$$

Dechlorination processes are approximated as first-order reactions neglecting the effect of biomass growth and inhibitors. According to biotic reductive dechlorination pathways, PCE ($i = 1$) reacts to produce TCE ($i = 2$), TCE reacts to produce three daughter species, cis-1,2-DCE ($i = 3$), trans-1,2-DCE ($i = 4$), and 1,1-DCE ($i = 5$) simultaneously, while the three DCEs further react to produce VC ($i = 6$), and VC reacts to produce ETH ($i = 7$) that reacts to produce CO_2 and H_2O. Furthermore, a result of the biodegradation of CEs is chloride (Cl^-) ($i = 8$): complete dechlorination gives rise to 4 mol of chloride for each mole of PCE degraded (Semprini et al. 1990; Wiedemeier et al. 1996). The reaction network matrix Λ and Λ' depicts the coupling between the chlorinated solvents and their degradation products. In a similar way to the dechlorination model reported in Sun et al. (2004), Λ is an 8×8 matrix expressed as:

$$\Lambda = \begin{bmatrix} -\lambda_1 & 0 & 0 & 0 & 0 & 0 & 0 & 0 \\ Y_{1\to2}\lambda_1 & -\lambda_2 & 0 & 0 & 0 & 0 & 0 & 0 \\ 0 & Y_{2\to3}\lambda_2 a_3 & -\lambda_3 & 0 & 0 & 0 & 0 & 0 \\ 0 & Y_{2\to4}\lambda_2 a_4 & 0 & -\lambda_4 & 0 & 0 & 0 & 0 \\ 0 & Y_{2\to5}\lambda_2 a_5 & 0 & 0 & -\lambda_5 & 0 & 0 & 0 \\ 0 & 0 & Y_{3\to6}\lambda_3 & Y_{4\to6}\lambda_4 & Y_{5\to6}\lambda_5 & -\lambda_6 & 0 & 0 \\ 0 & 0 & 0 & 0 & 0 & Y_{6\to7}\lambda_6 & -\lambda_7 & 0 \\ Y_{1\to8}\lambda_1 & Y_{2\to8}\lambda_2 & Y_{3\to8}\lambda_3 & Y_{4\to8}\lambda_4 & Y_{5\to8}\lambda_5 & Y_{6\to8}\lambda_6 & 0 & 0 \end{bmatrix} \tag{17}$$

where λ_i represent the first-order decay rate of the i-th species, $Y_{i\to j}$ is the stochiometric conversion factor for reductive dechlorination from i-th to j-th species, a_i $i = 3, 4, 5$ are the product distribution factors for reduction of TCE. In an analogous manner it can be defined as the reaction network matrix Λ'.

A new approach has been developed in order to implement equilibrium adsorption, mass transfer and reductive dechlorination processes into the random-walk particle tracking. To each particle released into the domain the following state variables are assigned: x_p and y_p which indicate the x and y space coordinates respectively at time t; s_p which indicates whether the particle resides in the mobile ($s_p = 1$) or stagnant ($s_p = 0$) zone; i_p denotes the species associated with the particle ($i_p = 1,\ldots,8$). To each particle the values of velocity vector $\mathbf{v}$, the retardation factors $R_m^{i_p}$ and $R_{im}^{i_p}$, the capacity ratio β^{i_p} and the mass transfer coefficent α^{i_p} are associated, according to the particle position (x_p and y_p) and the associated species (i_p). An execution predictor correction scheme is used in the model. Particle position at time $t + 0.5\Delta t$ is predicted and the aforementioned variables are updated according to the new particle position and new value of i_p determined as explained in the following. Then the full time-step $t + \Delta t$ is computed.

Assuming that when the particles released at source are in the mobile zone, the transition probabilities associated with each particle, according to Salamon et al. (2006), can be written as:

$$P^{i_p}_{m\to m} = \frac{1 + \beta^{i_p}e^{-(1+\beta^{i_p})\alpha^{i_p}\Delta t}}{1 + \beta^{i_p}} \tag{18}$$

$$P^{i_p}_{im\to im} = \frac{\beta^{i_p} - \beta^{i_p}e^{-(1+\beta_i(x,y))\alpha_i(x,y)\Delta t}}{1 + \beta^{i_p}} \tag{19}$$

where $P^{i_p}_{m\to m}$ and $P^{i_p}_{im\to im}$ represent, respectively, the probability of the particle starting in the mobile zone and ending in the mobile zone, and the probability of the particle starting in the stagnant zone and ending in the stagnant zone.

The state variable s_p of each particle in the mobile zone associated with the species i is updated according to:

$$s_p(t + \Delta t) = \begin{cases} 1 \text{ if } Y < P^{i_p}_{m\to m} \\ 0 \text{ if } Y \geq P^{i_p}_{m\to m} \end{cases} \tag{20}$$

Whereas for the particle associated with the species i in the stagnant zone, s_p is updated according to:

$$s_p(t + \Delta t) = \begin{cases} 0 \text{ if } Y < P^{i_p}{}_{im \to im} \\ 1 \text{ if } Y \geq P^{i_p}{}_{im \to im} \end{cases} \tag{21}$$

where Y is a uniform random number between 0 and 1.

The particles in the mobile zone associated with the species i move in agreement with the random walk scheme, updating x_p and y_p in the following way:

$$x_p(t + \Delta t) = x_p(t) + \frac{v'_x}{R_m^{i_p}} \Delta t + Z_1 \sqrt{2 \frac{D_L}{R_m^{i_p}} \Delta t \frac{v_x}{|\mathbf{v}|}} - Z_2 \sqrt{2 \frac{D_T}{R_m^{i_p}} \Delta t \frac{v_y}{|\mathbf{v}|}} \tag{22}$$

$$y_p(t + \Delta t) = y_p(t) + \frac{v'_y}{R_m^{i_p}} \Delta t + Z_1 \sqrt{2 \frac{D_L}{R_m^{i_p}} \Delta t \frac{v_y}{|\mathbf{v}|}} - Z_2 \sqrt{2 \frac{D_T}{R_m^{i_p}} \Delta t \frac{v_x}{|\mathbf{v}|}} \tag{23}$$

With:

$$v'_x = v_x + \frac{\partial D_{xx}}{\partial x} + \frac{\partial D_{xy}}{\partial y} \tag{24}$$

$$v'_y = v_y + \frac{\partial D_{xy}}{\partial x} + \frac{\partial D_{yy}}{\partial y} \tag{25}$$

$$D_L = \alpha_L |\mathbf{v}| \tag{26}$$

$$D_T = \alpha_T |\mathbf{v}| \tag{27}$$

where Z_1 and Z_2 are two normally distributed random variables.

Note that, in order to take linear equilibrium adsorption processes into account, velocity and dispersion parameters are divided by the mobile retardation factor which is different for each particle according to the sorption characteristics of the associated species and its particle space position corresponding to a different value of the surface-area to volume ratio of the fracture system.

As known, the first-order kinetic model does not depend on the concentration distribution of the organic compounds in groundwater; therefore, the reaction processes can be split by the transport processes. The reductive dechlorination efficiency can be variable in space due to the changes of predominant electron-accepting processes. Screening of groundwater chemistry helps to determine the redox zonation. Then each redox zone can be characterised by a reaction network matrices. At time t, a number of particles n_p^t enter into the generic redox zone. Each particle enters with an initial value of i_p and, given that particle moves, s_p is equal to 1. Successively, each particle changes i_p by a random sampling procedure following a Markov chain model as discussed in the following.

At the set of particles n_p^t a column vector $\mathbf{m}_p^t$ is associated, containing the mass distribution of each species. At time $t + \Delta t$, $\mathbf{m}_p^t$ is updated according to the following governing equation representing the reaction processes:

$$\frac{\partial \mathbf{m}_p^t}{\partial t} = \Lambda \mathbf{m}_p^t \tag{28}$$

Equation (28) is solved using the implicit Euler scheme:

$$\mathbf{m}_p^t(t + \Delta t) = e^{(\Lambda \Delta t)} \mathbf{m}_p^t(t) \tag{29}$$

Once $\mathbf{m}_p^t$ is updated the state variable i_p of each particle is changed according to the transition probabilities. Figure 3a shows the graph representation of the possible transitions and Fig. 3b particle resampling of state variables i_p. Transition probabilities from one species to another in the time interval $(t, t + \Delta t)$ are related to the mass consumed per unit of mass (Sole-Mari et al. 2017):

$$\Delta m_i = \frac{\mathbf{m}_p^t(i)_t - \mathbf{m}_p^t(i)_{t + \Delta t}}{\mathbf{m}_p^t(i)_t} \tag{30}$$

The transition probabilities showed in Fig. 3 assume the following expressions:

for $i = 1, 3, 4, 5, 6$

$$\begin{aligned} P_{i \to i+1} &= \Delta m_i Y_{i \to i+1} \\ P_{i \to 8} &= \Delta m_i Y_{i \to 8} \\ P_{i \to i} &= 1 - P_{i \to i+1} - P_{i \to 8} \end{aligned} \tag{31}$$

for $i = 2$

$$\begin{aligned} P_{i \to i+1} &= \Delta m_i Y_{i \to i+1} \alpha_{i+1} \\ P_{i \to i+2} &= \Delta m_i Y_{i \to i+2} \alpha_{i+2} \\ P_{i \to i+3} &= \Delta m_i Y_{i \to i+3} \alpha_{i+3} \\ P_{i \to i+8} &= \Delta m_i Y_{i \to 8} \\ P_{i \to i} &= 1 - P_{i \to i+1} - P_{i \to i+2} - P_{i \to i+3} - P_{i \to 8} \end{aligned} \tag{32}$$

for $i = 7$

$$\begin{aligned} P_{i \to i+2} &= \Delta m_i \\ P_{i \to i} &= 1 - P_{i \to i+2} \end{aligned} \tag{33}$$

Random resampling occurs step by step starting from the particles having $i_p = 1$ and ending with the particles having $i_p = 7$. In this way, for the i-th species the discrete cumulative distribution function CDF is determined by means of the transition probabilities associated with the i-th species. For each particle having $i_p = i$, a uniform random number U, between 0 and 1, is generated, then the new value of state variable i_p will be taken according to $CDF^{-1}(U)$ (Fig. 3b).

At time $t + \Delta t$, some particles of n_p^t will be in the stagnant zone. Then two column vectors $\mathbf{m}_p^t$ and $\mathbf{m}'^t_p$ will be associated with n_p^t, containing the mass distribution of each species in the mobile zone and stagnant zone respectively. At time $t + 2\Delta t$, mass distribution vectors are updated according to Eq. (29) substituting Λ' with Λ for the determination of $\mathbf{m}'^t_p$. The state variable i_p of each particle is updated according to the random
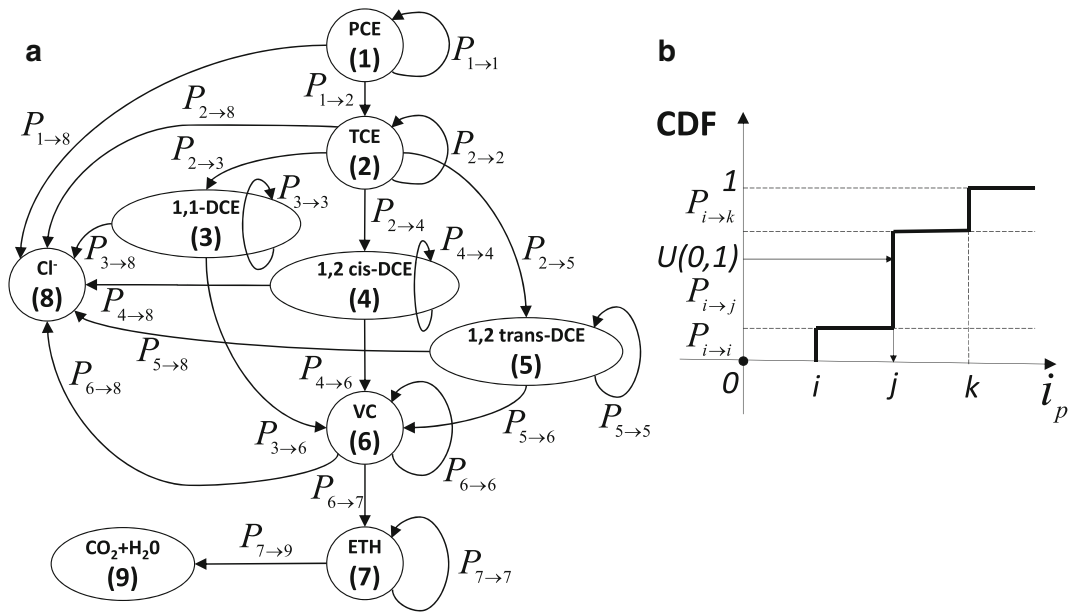
Fig. 3 **a** Graph representation of the possible transitions, **b** particle resampling of state variable i_p according to the cumulative distribution function (CDF) of the transition probabilities

resampling method using $\mathbf{m}_p^t$ for particle with $s_p = 1$ and $\mathbf{m}'^t_p$ for particle with $s_p = 0$.

For each species the solute concentration distribution can be obtained at the end of the simulation associating a regular grid to the domain with the cell size Δx^2 (L^2) and cell volume V (L^3) equal to the product between $n_f \times \overline{b}$ and Δx^2. Then the solute concentration for each cell is determined by means of the following equation:

$$C_i = n_p^i \frac{M_{tot}^i}{n_{tot}^i \times V} \tag{34}$$

where C_i ($M\,L^{-3}$) is the solute concentration of species i at the cell, n_p^i is the number of particles within the cell associated with the species i, M_{tot}^i (M) is the total solute mass of species i in the domain, and n_{tot}^i is the total number of particle i-th species in the domain.

Results

Flow field determination

Hydrogeological features of the study area have been analyzed in previous work (Cherubini et al. 2018). In particular, a 2D groundwater flow model has been set up on the basis of 98 long-term step drawdown tests, showing a variation of transmissivity in the study area in the range 10^{-5}–10^{-2} $m^2\,s^{-1}$. The 2D groundwater flow model has been set up using the finite difference numerical code MODFLOW with a constant cell size $\Delta x = 100$ m. The flow model has been calibrated and validated on the

basis of the hydraulic head measurement. Groundwater flows from SW to NE, characterized by the high value of the hydraulic head in the up-stream zones that decreases dramatically passing into the coastal zone. The observed trend of the hydraulic gradient is consistent with the aquifer transmissivity distribution detected in the site (Fig. 4).

Having determined the equivalent transmissivity and constructed the hydraulic head maps, the rough-walled parallel-plate model was set up on the basis of the experimental observations of conservative tracer transport in the study area reported by Masciopinto and Palmiotta (2016). A mixture of 1 m^3 of water with 5 kg of chlorophyll powder was injected into the wells with a constant flow rate of 2 L s^{-1} using an injection pipeline. Then the latter pipeline was removed and groundwater was sampled at regular time intervals via a sampling pump placed at the assigned water depth of 3 m into the well. Each water sample was stored in a plastic bottle and transported to a laboratory, where the water absorbance of the samples was determined. The measurement of tracer concentration in the borehole referred to a calibration curve previously determined in the laboratory using a spectrophotometer at a frequency of 405 nm.

Flow velocity field was calibrated by means of the results of point dilution tests carried out in the upstream zone (#1 well) and coastal zone (#2 well) where the long-term step drawdown pumping test showed a value of 9.5 and 3,715 m^2 day^{-1} of equivalent transmissivity for the upstream zone and coastal zone respectively.

Specific discharge has been determined by fitting the experimental chlorophyll concentration data with an analytical solution provided by Louis (1977):

Fig. 4 Contours of groundwater level (m asl; black curves), flow paths (gray curves) and hydraulic transmissivity (*T*) distribution for the study area. #1 and #2 are point-dilution-test locations, and #3 is the forced-gradient test location (black dots)
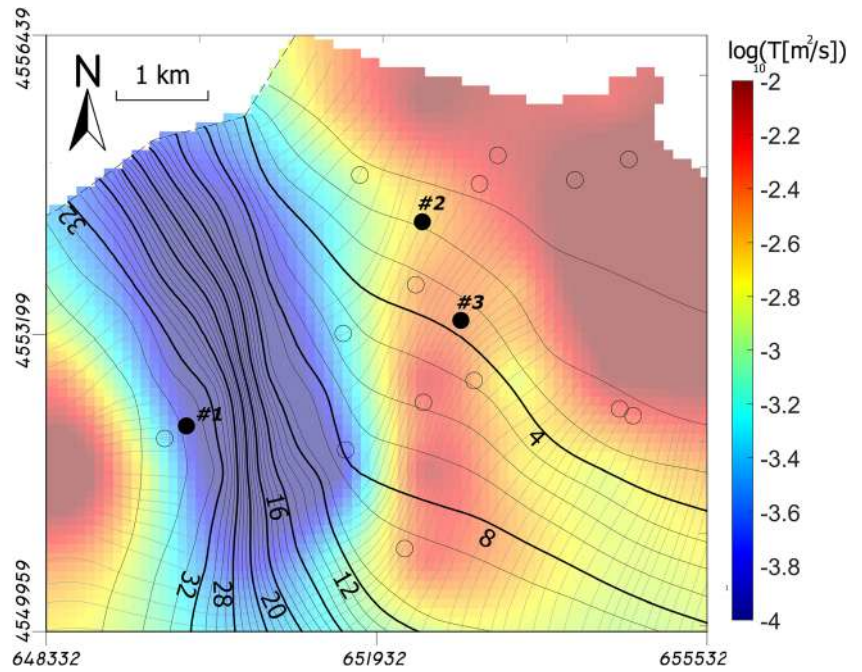
$$C = C_0 \exp\left(\frac{4}{r_0 L}\overline{q} \times t\right) \tag{35}$$

where C_0 (ML^{-3}) is the initial concentration of tracer at $t = 0$, C (ML^{-3}) is the concentration of tracer at time t, r_0 (L) is the well radius, L (L) is the length of well screen. Values of specific discharge of 1.0 and 3.8 m^2 day^{-1} have been estimated respectively for the upstream and coastal zone (Figs. 4 and 5). The ratio between the specific discharge and flow velocity derived by the numerical model represents the specific void
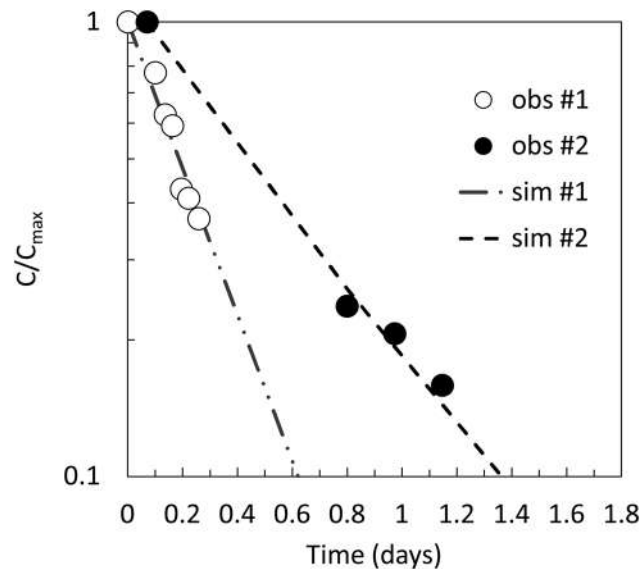
Fig. 5 Interpretation of the point dilution tests. Comparison between the observed-tracer-concentration (Masciopinto and Palmiotta 2016) and theoretical-concentration (Eq. 35) evolution versus time

area available for the flow equal to the product $n_f \times \overline{b}$. Assuming a value of n_f, the flow velocity field is determined according to the recursive equations (Eqs. 6–9). The effective porosity of the aquifer θ_m can be derived by the ratio between $n_f \times \overline{b}$ and the average aquifer thickness B (L). Figure 6 shows the relationships between the number of parallel fractures of the flow model and the effective porosities of the upstream and downstream zones that increase, in a potential way, as the number of parallel fractures increases. A number of parallel plates of 20 is consistent with a value of effective porosity of ~0.3% found by Masciopinto and Palmiotta (2016).

Figure 7a,b shows the main flow path ($n_f = 20$) starting from the source of contamination, for the linear flow model (assuming the cubic law is valid) and nonlinear flow model, respectively. The figure evidences how the nonlinear flow model estimates a lower value of flow velocity than the linear model, and the particles reach the coast from the source with a delay of 20 days (relative to the linear flow model).

Transport and biodegradation processes of chlorinated ethenes

A site-specific transport model including the effect of dual porosity and reductive dechlorination of CEs presented in the previous section has been set up on the basis of flow-field determination. The mass transfer coefficient and the capacity ratio have been estimated through interpretation of the experimental forced gradient breakthrough curve (BTC) derived by Masciopinto and Palmiotta (2013). The forced
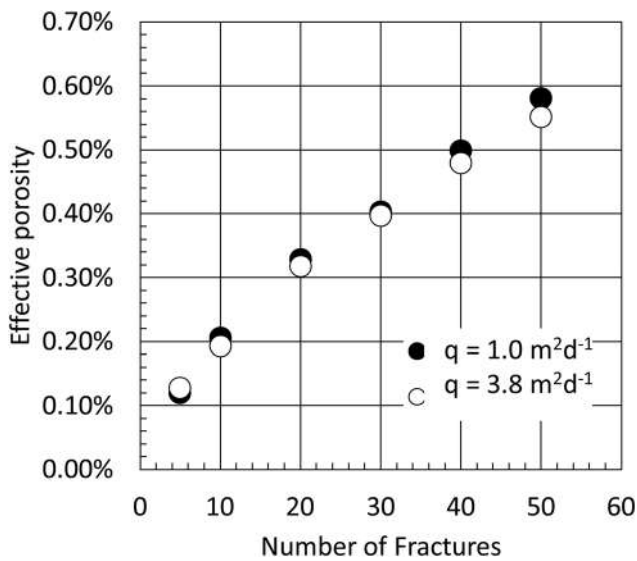
Fig. 6 Relationship between the number of plates and effective porosity estimated at #1 well location (black dots) and #2 well location (white dots)

gradient test was conducted at the Istituto di Ricerca sulle Acque (IRSA) field test site (location #3). The chlorophyll mixture was injected into the injection well, located at a distance of 10 m from pumping well where groundwater was being extracted with a flow rate of 72.5 L s^{-1}. There was maximum tracer concentration of the withdrawal of 300 µg L^{-1}. The experimental BTC was fitted with the theoretical BTC, derived by the random-walk transport model presented in the previous section, without retardation and reductive dechlorination (Fig. 8). A value of 4.10×10^{-3} s^{-1} and 0.49 was estimated for the mass transfer coefficient and the capacity ratio for conservative solute considering a mean convective

flow velocity of 0.02 m s^{-1} and a longitudinal dispersion of 0.26 m. At this scale of investigation (distance between injection and extraction well equal to 10 m) and forced flow regime, the effect of dual porosity is evident, characterized by an early arrival and long tailing, reproduced adequately by the implemented transport model.

The porosity of the stagnant and recirculation zones can be derived by the product between the capacity ratio and the effective porosity reaching a value of 0.16%. The estimated value of the mass transfer coefficient and the capacity ratio is consistent with the experiments at bench scale conducted by Cherubini et al. (2013b, 2014), where the capacity ratio showed a value of 0.5 and a dependence between the mass transfer and Reynolds number was detected via a power function (Eq. 16). A value of 50 m was chosen for longitudinal dispersivity on the basis of the scale-dependence relationship reported in Beims (1983) with a ratio of 10 between lateral dispersivity and longitudinal dispersivity.

Processes of sorption to fracture walls are due to the presence of organic carbon and iron oxides in the thin fracture coating of red soil. Capursi (2011) conducted batch experiments on sorption potential of CEs on red soil samples of the study area, and found, based on a linear sorption model, a value of apparent organic carbon fraction determined by the ratio between the experimental distribution coefficients and the partition coefficient of each species equal to 0.0681%. Assuming a mean value of θ equal to 3%, a geometric factor δ equal to 0.01, and a bulk density of the reactive soil of 1.260 g cm^{-3}, a value of the internal specific surface area of the matrix rock γ is estimated equal to 0.4762 cm^2 g^{-1}. The generic stoichiometric conversion factor $Y_{i \to j}$ is determined by the ratio between the molecular weight M (g × mol^{-1}) of the
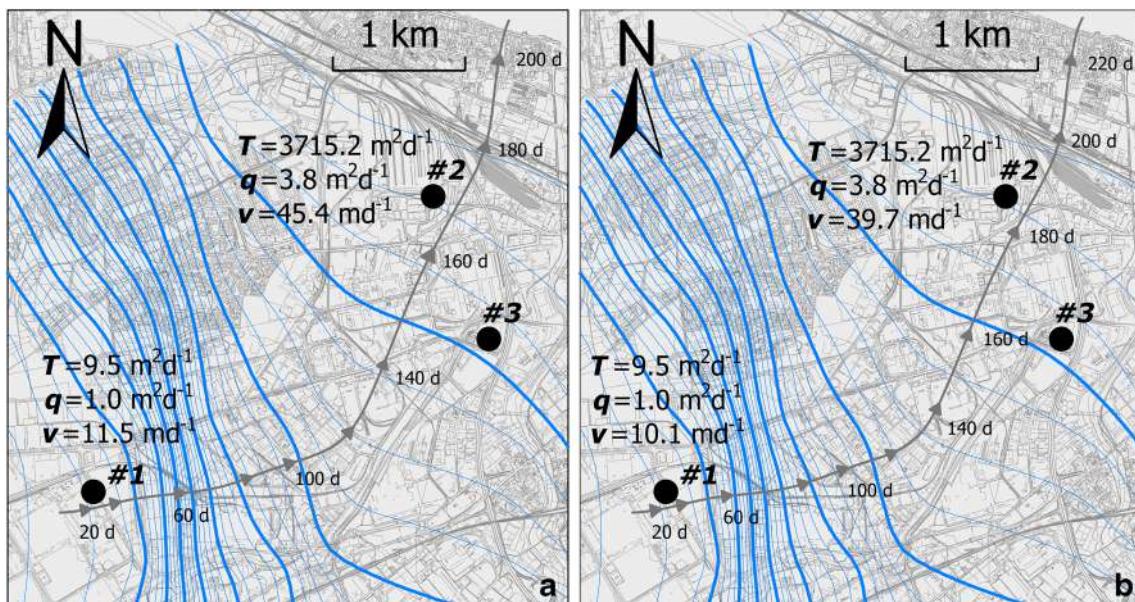
Fig. 7 Main flow path from the source, with $n_f = 20$, obtained using **a** the linear flow model (cubic law) and **b** nonlinear flow model (Darcy–Weisbach equation)
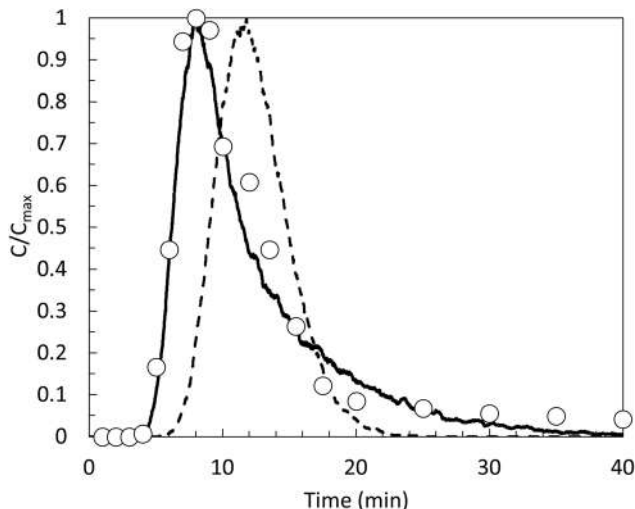
Fig. 8 Forced-gradient test interpretation. Comparison between observed BTC (white dots) (Masciopinto and Palmiotta 2013) and simulated BTCs: best fit result with $\alpha = 4.1 \times 10^{-3}$ and $\beta = 0.49$ (bold curve); BTC with $\alpha = 10^2$ s^{-1} correspond to a fast exchange between mobile and stagnant zones, and the solute moves with an effective porosity equal to the total porosity (dotted curve). The comparison between the forced gradient test result and the Eq. (16) is reported in the electronic supplementary material (ESM)

the mass rate M_0 [MT^{-1}] and the particles' mass distribution between the species $\mathbf{f}_p$ has been associated. Then the column vector $\mathbf{m}_p^t$ containing the mass distribution of each species associated with the particle was initialised as:

$$\mathbf{m}_p^t = M_0 \cdot \mathbf{f}_p \cdot \Delta t \qquad (36)$$

At time $t + \Delta t$, the column vectors $\mathbf{m}_p^0, \ldots, \mathbf{m}_p^t$ are updated according to Eq. (29) and the related transition probabilities were determined by means of Eqs. (31)–(33). State variable i_p of each particle associated with $\mathbf{m}_p^0, \ldots, \mathbf{m}_p^t$ was updated using random resampling scheme (Fig. 3). Successively, according to i_p, the velocity vector, the retardation factors, the capacity ratio and the mass transfer coefficient associated with each particle were determined and they were used to update state variable s_p according to Eqs. (20)–(21) and state variables x_p and y_p according to Eqs. (22) and (23).

A time step $\Delta t = 1$ day was chosen. The simulation continued until the quasi-steady-state condition had been reached; in order words, as long as the total number of particles for each species within the domain remains almost constant over time. Quasi-steady-state condition was obtained in a simulation period of more or less 10 years with a total number of particles released into the domain of ~10,000,000.

Three cases have been simulated: (case I) the particles' mass distribution $\mathbf{f}_p$ at source between the species is fixed proportionally to its concentration detected in the hot spot; (case II) $\mathbf{f}_p$ is fixed as 100% PCE; case III) $\mathbf{f}_p$ can change according to the best fit between the observed and simulated concentrations.

For the case 1, the first-order decay coefficients have been set to zero in order to highlight the effect of the physical transport processes (advection, dispersion, sorption and mass transfer), whereas in the cases II and III the dechlorination model is active and the first-order decay coefficients and the product distribution factors of the TCE reduction (α_3, α_4 and α_5) have been estimated through the comparison between the observed concentrations of CEs along the main flow path and the simulated ones.

species i and j respectively. Table 1 reports the values of molecular weight (M), partition coefficient (K_{OC}), distribution coefficient (K_d) and the surface distribution coefficient (K_a) for each considered species.

Groundwater chemistry investigations suggest the use of a unique redox zone for the whole domain. In order to simplify the estimation of the first-order decay rates, reaction network matrices have been assumed equal for the mobile and stagnant zones. Transport and reductive dechlorination simulations start from the condition of no contamination (the number of particles released into the domain at $t = 0$ is zero). A constant mass-loading boundary condition was imposed at the source located in correspondence with the potential source area (latitude/longitude: $N = 4,552,039$, $E = 649,610$). At time t, a constant number of $n_p^t = 20,000$ particles was released into the mobile domain at the potential source area. For these particles,

Table 1 Parameters for chlorinated ethenes and their degradation products. Molecular wheight (M), partition coefficient (K_{OC}), distribution coefficient (K_d), surface distribution coefficient (K_a)

Species	i_p	M (g Mol^{-1})	K_{oc} (ml g^{-1})	K_d (ml g^{-1}) $\times 10^3$	K_a (cm) $\times 10^3$
PCE	1	165.80	218	148	31.2
TCE	2	131.40	101	69	14.4
1,1-DCE	3	96.94	60	41	8.6
cis-1,2-DCE	4	96.94	54	37	7.7
trans-1,2-DCE	5	96.94	54	37	7.7
VC	6	62.50	57	39	8.1
ETH	7	28.05	13	9	1.8
Cl$^-$	8	35.45	–	–	–

Fig. 9 Comparisons between the simulated concentration distributions ($\mu g\ L^{-1}$) of chlorinated ethenes and their products along the main flow path for: scenario 1 (bold black curve), scenario 2 (bold gray curve), scenario 3 (red curve) and observed concentrations in monitoring wells that cross the main flow path ($\mu g\ L^{-1}$), relative to the monitoring periods March–May 2014 (black dot) and October–December 2014 (white square). **a** PCE, **b** TCE, **c** 1,2–DCE, **d** 1,1–DCE, **e** VC, **f** Cl$^-$ and ethylene (ETH). The distance along the main flow path associated with the generic monitoring well is measured in correspondence to the intersection between the main flow path and its perpendicular straight line passing through the generic monitoring well
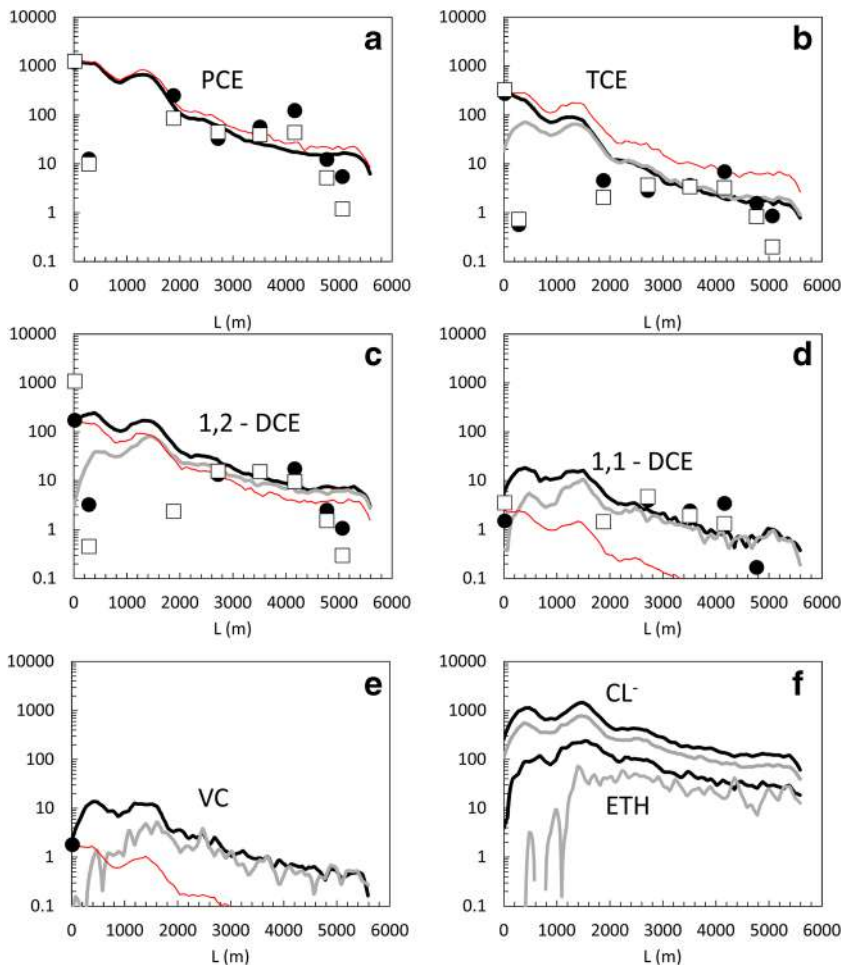
Given that the groundwater chemistry investigation reported only the sum of the cis 1,2-DCE and trans 1,2-DCE, the two species have been lumped in the model. Then the sum of α_4 and α_5 has been determined.

At the end of the simulations, the concentration distribution map of each species was determined by Eq. (34) and the corresponding concentration distributions along the main flow path were mapped. The latter were compared with the observed data from wells crossing the main flow path. The root mean square error between the observed data and simulated data was used as the criterion to reach the best fit, in order to estimate (1) mass loading rate, (2) particle mass distribution at source and (3) the first-order decay rates and the product distribution factors for reduction of TCE.

Figure 9 shows the comparison between the observed and simulated scenarios of contamination for both considered cases along the main flow path. The estimated parameters are reported in Tables 2 and 3. Figures 10, 11, 12, and 13 show the steady-state-simulated particle distribution and simulated/observed concentration of CEs and their reductive products relative to case III.

Discussion

The present work demonstrates that the proposed conceptualisation of the fractured, karst limestone of Bari aquifer gives a good representation of the flow field, consistent with the flow observed at the study site. The estimated number of horizontal rough-walled plates ($n_f = 20$) leads to a mean aperture

Table 2 Mass rate at source and particle mass distribution at source for each considered case

Parameter	Case I	Case II	Case III
Mass rate at source, M_0 (g day^{-1})	14	25	35
Particle fraction at source, f_p (%)			
PCE	63.8	100.0	57.0
TCE	21	0	36.0
1,1-DCE	0	0	0
1,2-DCE, cis and trans	14.9	0	7.0
VC	0.1	0	0
ETH	0	0	0

14

Table 3 First-order decay rate (λ), half-life ($t_{1/2}$) and distribution factors for TCE estimated by the model

| Species	λ (day^{-1})	$t_{1/2}$ (day)	Distribution factor for TCE
PCE	0.001	693	–
TCE	0.008	87	–
1,2-DCE cis and trans	0.003	231	–
1,2-DCE cis and trans ($a_4 + a_5$)	–	–	0.9
1,1-DCE	0.003	231	–
1,1-DCE (a_3)	–	–	0.1
VC	0.03	23	–
ETH	0	–	–

distribution in the range of 130–1,390 μm, which is consistent with those found by Masciopinto et al. (2017) at the field site through inverting the solution of the steady radial water flow to a well during pumping. The corresponding Reynolds number distribution is in the range of 0.003–2.119. Anyway, the analysis of the travel time along the main flow path, starting from the potential source area, evidences a discrepancy between the linear and nonlinear flow assumption in terms of travel time of 10%. This aspect discloses the fact that, under a cleanup strategy based on a pumping well that involves the

fractured limestone aquifer of Bari, the discrepancy between the linear and nonlinear flow assumption could become more relevant. This consideration is consistent with the finding of Masciopinto et al. (2010) which shows that at the field site, nonlaminar resistance cannot be neglected. The effect of nonlaminar resistance can produce relevant deviations of the groundwater velocity estimations and consequently in the results of simulation of contaminated transport.

At this scale of investigation, equilibrium between the mobile and stagnant zones has been reached within the grid cell

Fig. 10 Steady-state-simulated-particle distribution and simulated/observed concentration distributions as $\log_{10}(\mu g\ L^{-1})$ relative to case 3 and observed concentration as $\log_{10}(\mu g\ L^{-1})$ for: **a** PCE particle distribution, **b** PCE concentration distribution, **c** TCE particle distribution, **d** TCE concentration distribution
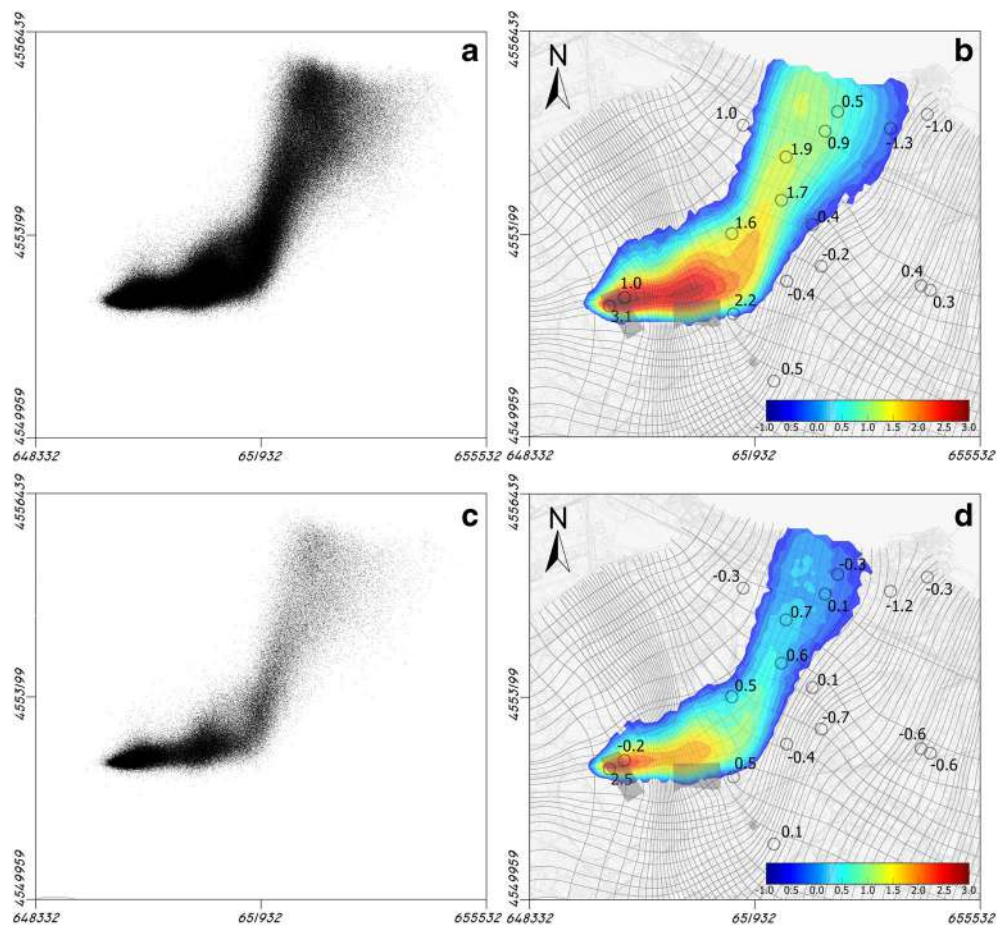
Fig. 11 Steady-state-simulated-particle distribution and simulated/observed concentration distributions as $\log_{10}(\mu g\ L^{-1})$ relative to case 3 for **a** 1,2-DCE particle distribution, **b** 1,2-DCE concentration distribution, **c** 1,1-DCE particle distribution, **d** 1,1-DCE concentration distribution
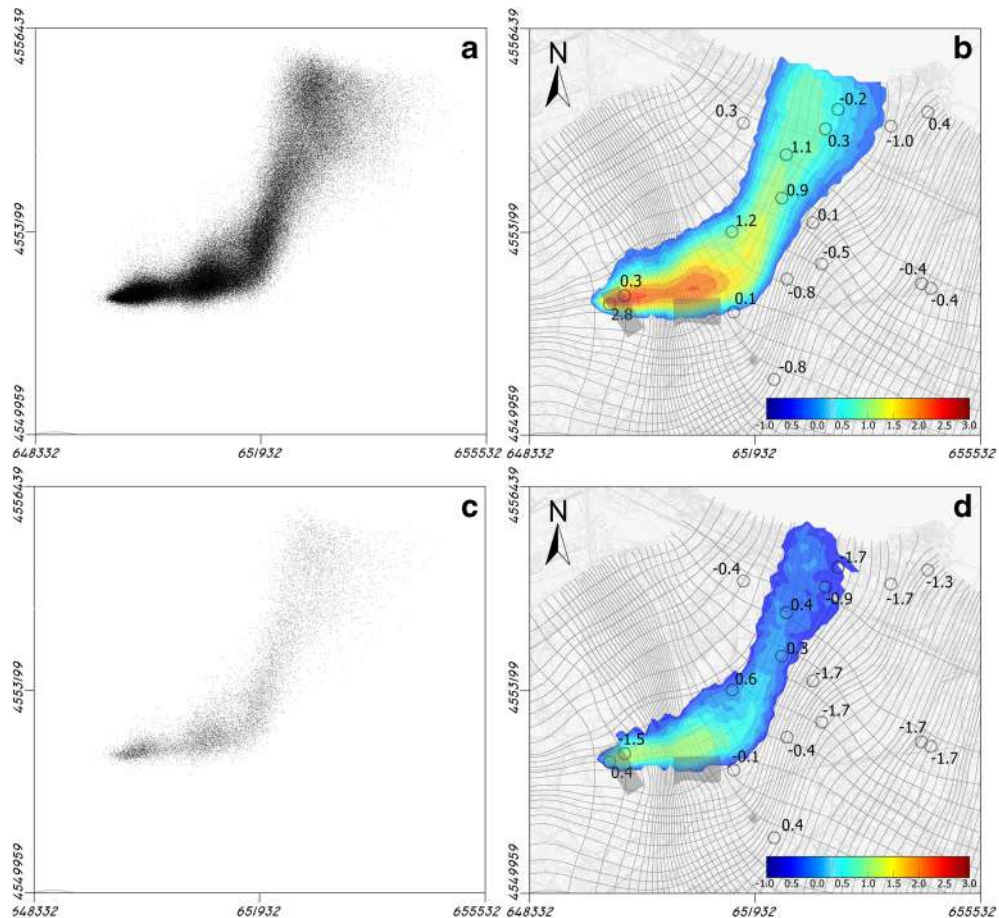
size ($\Delta x = 100$ m). The length scale required to reach the equilibrium given by the ratio between the velocity module and mass transfer coefficient (Steefel 2008) presents a maximum value of 0.75 m. This means that, under natural gradient conditions, the contamination propagates with an effective porosity equal to total porosity. In this way, 43% of total particles associated with the CEs present in the domain under quasi-steady-state conditions resulted in a stagnant zone, and 26% of the particles are associated with PCE. This finding emphasizes the persistence of the CEs. Pumping wells change the flow field, giving rise to nonequilibrium conditions between mobile and stagnant zones. Then the contaminant propagation changes behaviour, characterised by an early arrival and long tailing as observed in the forced gradient test conducted in the study area by Masciopinto and Palmiotta (2012). This result shows the persistence of CEs after aquifer remediation. In agreement with Mutch et al. (1993), the stagnant zones tend to retard contaminant plume propagation though the fractured-rock aquifer, increasing the difficulty of purging contamination from the groundwater.

The first-order decay rates estimated by the model indicate a limited effect of reductive dechlorination processes. PCE shows a relative low value of first-order decay rate, consistent with the transport of PCE at long distance. The degradation rate of TCE appears significant compared to the effect of only physical transport processes (case I) which overestimate the concentration distribution; in contrast, the dilution effect underestimates the concentration of 1,2-DCE and 1,1-DCE, and this means that DCE is degraded more slowly than TCE. Vinyl chloride was detected only at source and near to the coast at concentrations over the minimum detection limit ($0.25\ \mu g\ L^{-1}$) and at a concentration much lower than other CEs. The highest VC concentration is $2.1\ \mu g\ L^{-1}$. The model overestimates VC concentration in both cases II and case III. Iron (Fe^{3+}) reducing conditions may have favored the oxidation of DCE and VC to carbon dioxide, explaining the lower concentration of VC (Bradley et al. 1998).

Iron-reducing conditions are consistent with the detected VC concentrations, which are much lower than those of DCE or TCE, and by the persistence of PCE. Under this scenario, it is reasonable to think that nitrate contamination occurred after CEs contamination, inhibiting both CEs' natural attenuation and Fe^{3+} reduction.

This scenario is also consistent with an abiotic reaction that could involve the process of dehalogenation of CEs (Haderlein and Pecher 1999; McCormick et al. 2002), explaining the reductive dechlorination scenario under nitrate reducing conditions. Magnetite and pyrite are present in the

Fig. 12 Steady-state-simulated-particle distribution and simulated/observed concentration distributions as $\log_{10}(\mu g\ L^{-1})$ relative to case III for **a** VC particle distribution, **b** VC concentration distribution, **c** ETH particle distribution, **d** ETH concentration distribution
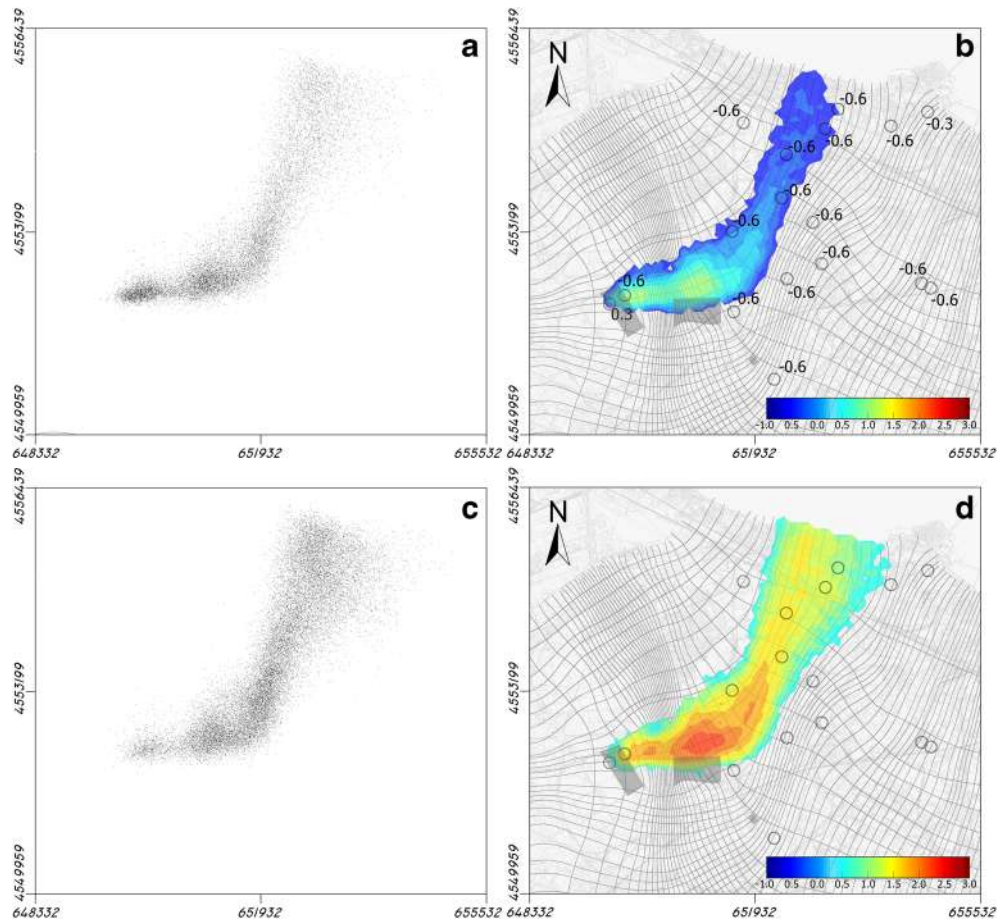
thin fracture coating (red soil), and, as demonstrated in Butler and Hayes (1999), Butler and Hayes (2000), Lee and Batchelor (2002), these minerals can favor the abiotic degradation of CEs.

The particle-based model also computed the distribution of chloride produced by the reductive dechlorination process. Chloride concentration is of the order of magnitude of 1,000 $\mu g\ L^{-1}$ (28.20 $\mu M\ L^{-1}$), much lower than the excess of chloride with respect to the sodium detected at the site. The

chloride contamination could have had a different source (i.e. sewage contamination). Except for that associated with VC, the estimated first-order decay rate of chloride assumes a relatively low value, although consistent with the literature values (Wilson et al. 1996; Yager 2002).

The developed particle-based model demonstrates the ability to represent adequately the implemented reaction pathways. Furthermore, no limitation on the size of the time step is needed, concerning the linear sorption process. To each

Fig. 13 Steady-state-simulated-particle distribution and simulated/observed concentration distributions as $\log_{10}(\mu g\ L^{-1})$ relative to case III for **a** Cl$^-$ particle distribution, **b** Cl$^-$ concentration distribution
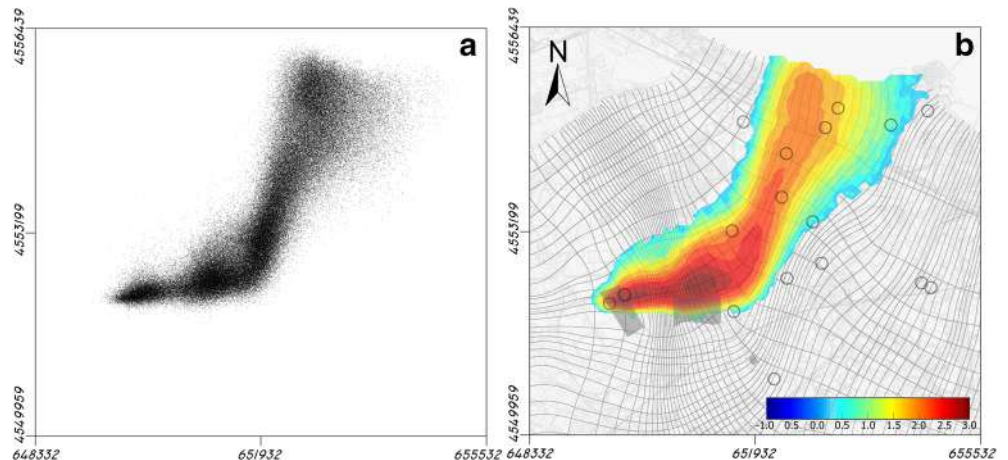
particle is associated a retardation factor depending on the single species and by the particle position in the space at time t and $t + \Delta t$ according to the predictor correction scheme. Contamination is viewed as a set of plumes formed by several particles, characterized by the fact that they enter a generic redox zone at a specific time. To these particles are linked a bin containing the total mass of the considered species involved in the simulated chemical reactions associated with these particles. The particles change species according to the evolution of this mass distribution in time. In this manner, parent species can be transformed into one or more daughter species (as demonstrated with the chloride and DCEs) and the mass budget is always satisfied. Transport simulation indicates that the information concerning the hydrogeology and the contaminant distribution at the site is coherent. The simulated plume and observed concentration of CEs is consistent, except for VC where the model overestimates VC concentration. Anyway, a limit of the VC half–life equal to 23 days has been imposed. Transport simulations depict well the concentration distribution, reflecting the heterogeneity of the aquifer, though the transport simulations are not able to represent the irregular shape of the detected contaminant distribution. The concentration at the well located immediately downgradient from the hot spot presents a concentration lower than the simulated ones, and the well located more southerly presents a concentration systematically higher than expected especially for the higher-chlorinated CEs. As shown in Cherubini et al. (2018), an explanation can be attributable to the presence of a watershed in correspondence to the hot-spot area, as demonstrated by the flow path lines where a change of direction in correspondence of the source is highlighted. Furthermore, the anticline affecting the Calcare di Bari formation gives rise to a local anisotropy of the fractured media with the SES–NNW main direction perpendicular to the anticline axis.

The main uncertainty in estimating the biodegradation rates and predicting the fate of CEs at the site is represented by the mass of nonaqueous phase liquid (NAPL) and its composition. The hypothesis relative to case II, where the NAPL mass fraction is equal to 100% PCE, does not appear to be consistent with the CEs concentration distribution at source. A spill of several CEs at source could have occurred, together with the possible geochemical and biological processes influencing the CEs in the NAPL, as demonstrated by the thermal anomalies at the hot-spot area. Furthermore, NAPL release could have occurred at different times and in different modalities, thus the hypothesis of continuous source could be restrictive.

Conclusions

The present study is aimed at analyzing the scenario of groundwater contamination by CEs of the industrial area of Bari (Italy) in a fractured, karstic limestone aquifer. Starting

from previous studies, the reliability of groundwater flow and transport models has been improved by analyzing literature data concerning experimental BTCs derived by point-dilution and forced-gradient tests conducted in the study area.

A new random-walk particle-tracking algorithm, incorporating velocity-dependent mass transfer between mobile and stagnant zones, linear adsorption processes and reductive dechlorination pathways, has been developed in order to simulate the quasi-steady-state scenario of contamination. The model adequately reproduces the transport and fate of CEs and their products. The uncertainty and limitation of the implemented model can be attributed to the hypothesis of a constant source in terms of mass loading rate and to the presence of local anisotropy of the fractured medium in correspondence of the hot-spot area, where a local discrepancy between the observed and simulated concentrations is highlighted.

Except for the vinyl chloride, the estimated first-order decay rate assumes a relatively low value, although consistent with the literature values (Wilson et al. 1996). The first-order decay rates found are consistent with the mildly reducing conditions detected in the study area, as the result of NO_3^- and Fe^{3+} reduction. Furthermore, the presence of magnetite and pyrite in the thin fracture coating (red soil) may have played a role in abiotic degradation of the CEs.

Given the obtained scenario of dechlorination, the use of monitored natural attenuation (MNA) as a cleanup strategy is not recommended for the study area, as it will not lead to the complete degradation of the CEs and there will be persistence of the contaminant plume in the aquifer. In all, 43% of the total particles associated with CEs lies in the stagnant zone. A possible alternative to MNA could be the implementation of ENA together with reduction in size of the hot-spot area at the source.

The developed site-specific particle-based reactive transport model represents a valid tool to predict contaminant migration and attenuation over time. The model can be used to estimate the mass of contaminant at source and the degradation rates, evaluating the convenience of the monitored natural attenuation method as a cleanup strategy. Future scenarios might consider the particle-based model in terms of both biotic and abiotic reaction pathways and the possibility of implementation of redox zones characterized by more complex kinetics corresponding to higher contaminant concentrations.

References

Beims U (1983) Planung, Dürchfuhrung und Auswertung von Gütepumpversuchen, Geohydrodynamische Erkundung [Planning,

implementation and evaluation of quality pumping tests, geohydrodynamic exploration]. ZAG 29(10):482-490

Benson DA, Bolster D (2016) Arbitrarily complex chemical reactions on particles. Water Resour Res 52:9190–9200. https://doi.org/10.1002/2016WR019368

Billi A (2005) Attributes and influence on fluid flow of fractures in foreland carbonates of southern Italy. J Struct Geol 27:1630–1643. https://doi.org/10.1016/j.jsg.2005.05.001

Borgia GC, Bortolotti V, Masciopinto C (2002) Valutazione del contributo della porosità effettiva alla trasmissività di acquiferi fratturati con tecniche di laboratorio e di campo [Evaluation of the contribution of the effective porosity to the transmissivity of fractured aquifers with laboratory and field techniques]. IGEA 17:31–43

Bradley PM, Chapelle FH, Wilson JT (1998) Field and laboratory evidence for intrinsic biodegradation of vinyl chloride contamination in a Fe(III)-reducing aquifer. J Contam Hydrol 31:111–127. https://doi.org/10.1016/S0169-7722(97)00058-2

Bradley PM, Lacombe PJ, Imbrigiotta TE, Chapelle FH, Goode DJ (2009) Flowpath independent monitoring of reductive dechlorination potential in a fractured rock aquifer. Groundw Monit Remediat 29:46–55. https://doi.org/10.1111/j.1745-6592.2009.01255.x

Burnell DK, Mercer JW, Faust CR (2014) Stochastic modeling analysis of sequential first-order degradation reactions and non-Fickian transport in steady state plumes. Water Resour Res 50:1260–1287. https://doi.org/10.1002/2013WR013814

Butler EC, Hayes KF (1999) Kinetics of the transformation of trichloroethylene and tetrachloroethylene by iron sulfide. Environ Sci Technol 33:2021–2027. https://doi.org/10.1021/es9809455

Butler EC, Hayes KF (2000) Kinetics of the transformation of halogenated aliphatic compounds by iron sulfide. Environ Sci Technol 34:422–429. https://doi.org/10.1021/es980946x

Capursi SR (2011) Adsorbimento di OCS su terra rossa e roccia calcarea [Adsorption of OCS on red earth and limestone]. PhD Thesis, Polytechnic of Bari, Faculty of Engineering, Department of Water and Chemistry, Bari, Italy

Cardenas MB, Slottke DT, Ketcham RA, Sharp JM Jr (2007) Navier-Stokes flow and transport simulations using real fractures shows heavy tailing due to eddies. Geophys Res Lett 34. https://doi.org/10.1029/2007GL030545

Cheng JM, Chen CX (2005) An integrated linear/non-linear flow model for the conduit-fissure-pore media in the karst triple void aquifer system. Environ Geol 47:163–174. https://doi.org/10.1007/s00254-004-1128-7

Cherubini C, Giasi CI, Pastore N (2012) Bench scale laboratory tests to analyze non-linear flow in fractured media. Hydrol Earth Syst Sci 16:2511–2522. https://doi.org/10.5194/hess-16-2511-2012

Cherubini C, Giasi C, Pastore N (2013a) Fluid flow modeling of a coastal fractured karstic aquifer by means of a lumped parameter approach. Environ Earth Sci 70:2055–2060. https://doi.org/10.1007/s12665-010-0851-5

Cherubini C, Giasi CI, Pastore N (2013b) Evidence of non-Darcy flow and non-Fickian transport in fractured media at laboratory scale. Hydrol Earth Syst Sci 17:2599–2611. https://doi.org/10.5194/hess-17-2599-2013

Cherubini C, Giasi CI, Pastore N (2014) On the reliability of analytical models to predict solute transport in a fracture network. Hydrol Earth Syst Sci 18:2359–2374. https://doi.org/10.5194/hess-18-2359-2014

Cherubini C, Pastore N, Rapti D, Giasi CI (2018) Numerical modeling of flow and transport in the Bari industrial area by means of rough walled parallel plate and random walk models. Hydrol Earth Syst Sci 22:5211–5225. https://doi.org/10.5194/hess-22-5211-2018

Cunningham JA, Mendoza-Sanchez I (2006) Equivalence of two models for biodegradation during contaminant transport in groundwater. Water Resour Res 42. https://doi.org/10.1029/2005WR004205

Dell'anna L, Fiore S, Laviano R (1985) The mineralogical, chemical and grain-size features of some clay deposits from Terra d'Otranto (Puglia, southern Italy). Geol Appl Idrogeol 20:111–123

Dou Z, Chen Z, Zhou Z, Wang J, Huang Y (2018) Influence of eddies on conservative solute transport through a 2D single self-affine fracture. Int J Heat Mass Transf 121:597–606. https://doi.org/10.1016/j.ijheatmasstransfer.2018.01.037

Engdahl NB, Benson DA, Bolster D (2017) Lagrangian simulation of mixing and reactions in complex geochemical systems. Water Resour Res 53:3513–3522. https://doi.org/10.1002/2017WR020362

Freeze RA, Cherry JA (1979). Groundwater. Prentice-Hall, Englewood Cliffs, NJ, 604 pp

Grassi D, Sdao F, Tadolini T (1986) Idrogeologia dell'area posta a cavallo della Murgia e del Tavoliere di Puglia [Hydrogeology of the area straddling the Murgia and the Tavoliere di Puglia]. Geol Appl Idro XXI:85–98

Guan J, Molz FJ, Zhou Q, Liu HH, Zheng C (2008) Behavior of the mass transfer coefficient during the MADE-2 experiment: new insights. Water Resour Res 44. https://doi.org/10.1029/2007WR006120

Haderlein SB, Pecher K (1999) Pollutant reduction in heterogeneous Fe(II)-Fe(III) systems. In: Mineral-water interfacial reactions. American Chemical Society, Washington, DC, pp 17–342

He YT, Wilson JT, Su C, Wilkin RT (2015) Review of abiotic degradation of chlorinated solvents by reactive iron minerals in aquifers. Groundw Monit Remediat 35:57–75. https://doi.org/10.1111/gwmr.12111

Henri CV, Fernàndez-Garcia D (2014) Toward efficiency in heterogeneous multispecies reactive transport modeling: a particle-tracking solution for first-order network reactions. Water Resour Res 50:7206–7230. https://doi.org/10.1002/2013WR014956

Henri CV, Fernàndez-Garcia D (2015) A random walk solution for modeling solute transport with network reactions and multi-rate mass transfer in heterogeneous systems: impact of biofilms. Adv Water Resour 86:119–132. https://doi.org/10.1016/j.advwatres.2015.09.028

Huitt JL (1956) Fluid flow in simulated fractures. AICHE J 2:259–264. https://doi.org/10.1002/aic.690020224

Kitanidis PK (1994) Particle-tracking equations for the solution of the advection-dispersion equation with variable coefficients. Water Resour Res 30:3225–3227. https://doi.org/10.1029/94WR01880

Lee W, Batchelor B (2002) Abiotic reductive dechlorination of chlorinated ethylenes by iron-bearing soil minerals: 1. pyrite and magnetite. Environ Sci Technol 36:5147–5154. https://doi.org/10.1021/es025836b

Lee SH, Yeo IW, Lee K-K, Detwiler RL (2015) Tail shortening with developing eddies in a rough-walled rock fracture. Geophys Res Lett 42:6340–6347. https://doi.org/10.1002/2015GL065116

Lee SH, Yeo IW, Lee K-K, Lee WS (2017) The role of eddies in solute transport and recovery in rock fractures: implication for groundwater remediation. Hydrol Process 31:3580–3587. https://doi.org/10.1002/hyp.11283

Lenczewski M, Jardine P, McKay L, Layton A (2003) Natural attenuation of trichloroethylene in fractured shale bedrock. J Contam Hydrol 64:151–168. https://doi.org/10.1016/S0169-7722(02)00090-6

Lima G, Parker B, Meyer J (2012) Dechlorinating microorganisms in a sedimentary rock matrix contaminated with a mixture of VOCs. Environ Sci Technol 46:5756–5763. https://doi.org/10.1021/es300214f

Louis C (1977) Suggested methods for determining hydraulic parameters and characteristics of rock masses, category II, Part 6, ISRM committee on standardization of laboratory and field tests

Lu C, Bjerg PL, Zhang F, Broholm MM (2011) Sorption of chlorinated solvents and degradation products on natural clayey tills. Chemosphere 83:1467–1474. https://doi.org/10.1016/j.chemosphere.2011.03.007

Maggiore M (1993) Aspetti idrogeologici degli acquiferi pugliesi in relazione alla ricarica artificiale [Hydrogeological aspects of Apulian aquifers in relation to artificial recharge]. Quad. 94, IRSA, Rome, pp 6.1–6.32

Manoli G, Chambon JC, Bjerg PL, Scheultz C, Binning PJ, Broholm MM (2012) A remediation performance model for enhanced metabolic reductive dechlorination of chloroethenes in fractured clay till. J Contam Hydrol 131:64–78. https://doi.org/10.1016/j.jconhyd.2012.01.004

Masciopinto C, Palmiotta D (2013) Flow and transport in fractured aquifers: new conceptual models based on field measurements. Transp Porous Media 96:117–133. https://doi.org/10.1007/s11242-012-0077-y

Masciopinto C, Palmiotta D (2016) A new method to infer advancement of saline front in coastal groundwater systems by 3D: the case of Bari (southern Italy) fractured aquifer. Computation 4. https://doi.org/10.3390/computation4010009

Masciopinto C, Volpe A, Palmiotta D, Cherubini C (2010) A combined PHREEQC-2/parallel fracture model for the simulation of laminar/non-laminar flow and contaminant transport with reactions. J Contam Hydrol 117:94–108. https://doi.org/10.1016/j.jconhyd.2010.07.003

Masciopinto C, Liso IS, Caputo MC, De Carlo L (2017) An integrated approach based on numerical modelling and geophysical survey to map groundwater salinity in fractured coastal aquifers. Water 9. https://doi.org/10.3390/w9110875

McCormick ML., Jung PT, Koster V, Hayes KF, Adriens P, Petrovski E, Skubal KL (2002) Assessing biotic and abiotic contributions to chlorinated solvent transformations in iron reducing and sulphidogenic environments. In: Groundwater quality: natural and enhanced restoration of groundwater pollution. Proceedings of the Groundwater Quality 2001 conference, Sheffield, UK, June 2001

Mutch RD, Scott JI, Wilson DJ (1993) Cleanup of fractured rock aquifers: implications of matrix diffusion. Environ Monit Assess 24:45–70. https://doi.org/10.1007/BF00568799

Nazridoust K, Goodarz A, Smith Duane H (2006) A new friction factor correlation for laminar, single-phase flows through rock fractures. J Hydrol 329(1–2):315–328

Novakowski KS, Canada CE, Canada NWRI (1999) The development of a conceptual model for contaminant transport in the dolostone underlying Smithville. Ontario, National Water Research Institute

Pérez-de-Mora A, Zila A, McMaster ML, Edwards EA (2014) Bioremediation of chlorinated Ethenes in fractured bedrock and associated changes in dechlorinating and nondechlorinating microbial populations. Environ Sci Technol 48:5770–5779. https://doi.org/10.1021/es404122y

Qian JZ, Chen Z, Zhan HB, Luo SH (2011) Solute transport in a filled single fracture under non-Darcian flow. Int J Rock Mech Min Sci 48:132–140. https://doi.org/10.1016/j.ijrmms.2010.09.009

Salamon P, Fernàndez-Garcia D, Gómez-Hernández JJ (2006) Modeling mass transfer processes using random walk particle tracking. Water Resour Res 42:1–14. https://doi.org/10.1029/2006WR004927

Sarkar S, Toksoz MN, Burns DR (2004) Fluid flow modeling in fractures. Earth Resources Laboratory Industry Consortia annual report, Earth Resour Lab MIT, Cambridge, MA, pp 1–41

Semprini L, Roberts PV, Hopkins GD, McCarty PL (1990) A field evaluation of in-situ biodegradation of chlorinated Ethenes: part 2, results of biostimulation and biotransformation experiments. Groundwater 28:715–727. https://doi.org/10.1111/j.1745-6584.1990.tb01987.x

Şimşir B, Yan J, Im J, Graves D, Löffler FE (2017) Natural attenuation in streambed sediment receiving chlorinated solvents from underlying fracture networks. Environ Sci Technol 51:4821–4830. https://doi.org/10.1021/acs.est.6b05554

Snow DT (1965) A parallel plate model of fractured permeable media. PhD Thesis, University of California, Berkeley, CA

Sole-Mari G, Fernàndez-Garcia D, Rodríguez-Escales P, Sanchez-Vila X (2017) A KDE-based random walk method for modeling reactive transport with complex kinetics in porous media. Water Resour Res 53:9019–9039. https://doi.org/10.1002/2017WR021064

Steefel C (2008) Geochemical kinetics and transport. In: Brantley S, Kubicki J, White A (eds) Kinetics of water-rock interaction. Springer, New York, NY. https://doi.org/10.1007/978-0-387-73563-4_11

Sun Y, Lu X, Petersen JN, Buscheck TA (2004) An analytical solution of tetrachloroethylene transport and biodegradation. Transp Porous Media 55:301–308. https://doi.org/10.1023/B:TIPM.0000013327.32136.52

Tiedeman CR, Shapiro AM, Hsieh PA, Imbrigiotta TE, Goode DJ, Lacombe PJ, DeFlaun MF, Drew SR, Johnson CD, Williams JH, Curtis GP (2018) Bioremediation in fractured rock: 1. modeling to inform design, monitoring, and expectations. Groundwater 56:300–316. https://doi.org/10.1111/gwat.12585

Tsang YW, Tsang CF (1987) Channel model of flow through fractured media. Water Resour Res 23(3):467–479. https://doi.org/10.1029/WR023i003p00467

Verce MF, Madrid VM, Gregory SD, Demir Z, Singleton MJ, Salazar EP, Jackson PJ, Halden UR, Verce A (2015) A long-term field study of in situ bioremediation in a fractured conglomerate trichloroethene source zone. Bioremediation J 19:18–31. https://doi.org/10.1080/10889868.2014.978836

Vingiani S, Di Iorio E, Colombo C, Terribile F (2018) Integrated study of red Mediterranean soils from southern Italy. CATENA 168:129–140. https://doi.org/10.1016/j.catena.2018.01.002

Waite ME, Ge S, Spetzler H, Bahr DB (1998) The effect of surface geometry on fracture permeability: a case study using a sinusoidal fracture. Geophys Res Lett 25:813–816. https://doi.org/10.1029/98GL00441

Wiedemeier TH, Swanson MA, Moutoux DE, Gordon EK, Wilson JT, Wilson BH, Kampbel DH, Hansen J, Haas P, Chapelle FH (1996). Technical protocol for evaluating natural attenuation of chlorinated solvents in groundwater. Air Force Center for Environmental Excellence, Technology Transfer Division, Brooks AFB, San Antonio, TX

Wilson JT, Kampbell DH, Weaver JW (1996) Environmental chemistry and the kinetics of biotransformation of chlorinated organic compounds in ground water. In: US Environmental Protection Agency, EPA/540/R-96/509, Symposium in natural attenuation of chlorinated organics in ground waters, Dallas, TX, September 11–13, 1996

Yager RM (2002) Simulated transport and biodegradation of chlorinated ethenes in a fractured dolomite aquifer near Niagara Falls, New York. US Geol Surv Water Resour Invest Rep 2000-4275

Yu R (2017) Laboratory evaluation of natural and enhanced remediation of chlorinated ethenes in fractured sandstone. PhD Thesis, Clemson University, Clemson, SC

Zhou Q, Liu H-H, Bodvarsson GS, Molz FJ (2006) Evidence of multi-process matrix diffusion in a single fracture from a field tracer test. Transp Porous Media 63:473–487. https://doi.org/10.1007/s11242-005-1123-9

Zimmerman RW, Bodvarsson GS (1996) Hydraulic conductivity of rock fractures. Transp Porous Media 23:1–30. https://doi.org/10.1007/BF00145263